

# Hyper-Kamiokande Outer Detector Light Injector System Technical Note

<sup>3</sup> Balint Bogdan<sup>1</sup>, Sam Jenkins<sup>\*1</sup>, Neil McCauley<sup>1</sup>, Liz Kneale<sup>2</sup>, Patrick Stowell<sup>2</sup>, Steve  
<sup>4</sup> Boyd<sup>3</sup>, Keith Jewkes<sup>3</sup>, Menai Lamers James<sup>3</sup>, Grace Hannaford<sup>3</sup>, and Ankush Mitra<sup>3</sup>

<sup>1</sup>University of Liverpool

<sup>2</sup>University of Sheffield

<sup>3</sup>University of Warwick

October 8, 2025

## **9** Contents

10	<b>0 Version history</b>	3
11	<b>1 Introduction</b>	4
12	<b>2 Light Injection System Overview and Requirements</b>	4
13	<b>3 OD PMT Saturation Study</b>	5
14	3.1 Diffuser Simulation . . . . .	6
15	3.2 Diffuser and OD Parameters . . . . .	7
16	3.3 Saturation Analysis . . . . .	8
17	3.4 Results . . . . .	9
18	<b>4 OD Collimator Studies</b>	11
19	4.1 Collimator Simulation . . . . .	11
20	4.2 Collimator Sensitivity Analysis . . . . .	13
21	4.3 Results . . . . .	13
22	<b>5 Diffuser Design</b>	15
23	5.1 ID Diffuser Hemisphere Design . . . . .	15
24	5.1.1 Inner Detector Diffuser Design . . . . .	15
25	5.1.2 Diffuser Profile Measurement System . . . . .	15
26	5.1.3 Diffuser Power Measurement System . . . . .	15
27	5.2 OD Diffuser Design . . . . .	18
28	<b>6 OD Diffuser Mounting System and Installation</b>	19

\*s.j.jenkins@liverpool.ac.uk

<b>29</b>	<b>7 Pulser Board</b>	<b>20</b>
30	7.1 Pulser Board Overview . . . . .	20
31	7.2 Physical Dimensions and Construction . . . . .	21
32	7.3 LED . . . . .	24
33	7.3.1 Overview . . . . .	24
34	7.3.2 Switching Circuit . . . . .	24
35	7.3.3 Switch Selection . . . . .	24
36	7.3.4 Testing . . . . .	25
37	7.4 LVDS to TTL Converter . . . . .	29
38	7.5 Power Supplies . . . . .	30
39	7.6 Connector . . . . .	31
40	7.7 Fibre Coupler . . . . .	32
41	7.8 Photon Yield Tests . . . . .	33
42	7.9 Production . . . . .	35
43	7.10 Changes Expected from v0.9 to v1.0 . . . . .	35
44	7.10.1 LED and Switching Circuit . . . . .	35
45	7.10.2 LVDS-to-TTL Converter . . . . .	35
46	7.10.3 Power Supplies . . . . .	35
47	7.10.4 Connector . . . . .	36
48	7.10.5 Fibre Coupler . . . . .	36
<b>49</b>	<b>8 Server Rack and Cooling</b>	<b>36</b>
<b>50</b>	<b>9 LED Monitoring</b>	<b>37</b>
<b>51</b>	<b>10 Control System for LEDs</b>	<b>37</b>
<b>52</b>	<b>11 Crate Electronics</b>	<b>38</b>
53	11.1 Overview . . . . .	38
54	11.2 Blade . . . . .	39
55	11.3 Backplane . . . . .	39
56	11.4 Eurocard . . . . .	40
<b>57</b>	<b>12 Summary</b>	<b>40</b>

<sup>58</sup> **0 Version history**

- <sup>59</sup> • v1 - First version released to the collaboration.

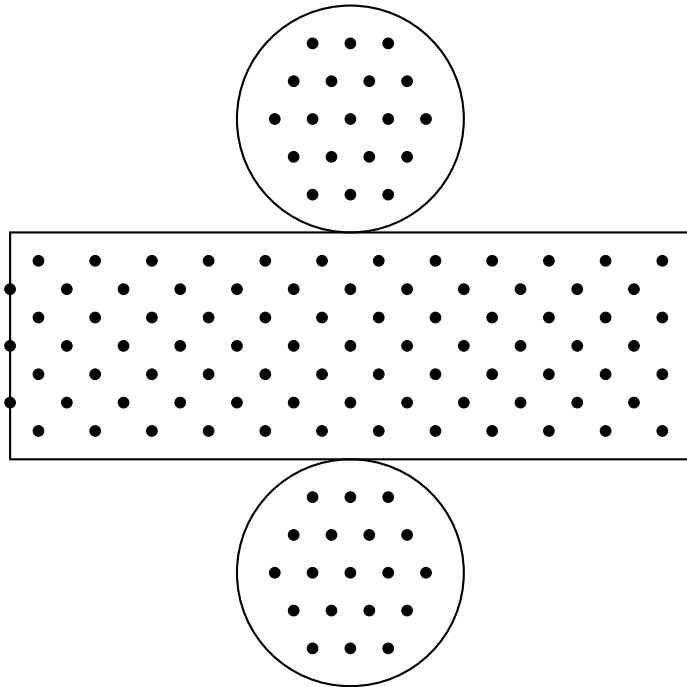
60 **1 Introduction**

61 Hyper-Kamiokande is a large scale water Cherenkov detector with two main sections, an  
62 inner detector (ID) and an outer detector (OD). The OD volume of Hyper-K is a one meter  
63 wide annular ring on the circumference of the detector. This space is designed to tag charged  
64 particles, such as cosmic ray muons or particles from interactions in the surrounding rock,  
65 entering the detector. In addition, the OD volume will be used as working space for instal-  
66 lation activities. Once complete, it will be optically separated from the ID volume, and will  
67 be instrumented with 3,600 outward facing 8 cm photomultipliers tubes (PMTs). These will  
68 each surrounded by wavelength shifting (WLS) plates to increase photocoverage.

69 In order to achieve the precision measurements Hyper-K aims to make, precise calibration  
70 of the detector is required. For the OD, a light injection (LI) system will be employed,  
71 allowing for known quantities of light to be injected into the detector region. This will  
72 consist of 122 diffusers and 12 collimators. The diffuser system, which is primarily described  
73 in this technical note, will be used to measure gain and timing properties of the OD PMTs,  
74 and will be powered by dedicated pulsed LED sources. The 12 OD collimators are identical  
75 to those used in the ID system, and will be integrated into the ID laser system. Full details  
76 on that system, along with investigations of the fibre optics that will be employed for the  
77 OD system, can be found in [1], although sensitivity studies to water parameters in the OD  
78 region are discussed in Section 4.

79 **2 Light Injection System Overview and Requirements**

80 The OD diffuser system will be composed of 122 bare diffusers, installed on the outward facing  
81 side of the PMT support structure. The proposed layout for this is shown in Figure 1, though  
82 in actuality there will be minor differences from this regular arrangement due to restrictions  
from other systems. These are arranged such that they illuminate roughly an equal number



83 Figure 1: Injector location map for OD diffuser positions. Locations are approximate and  
dependent on PMT/WLS plate locations.

84 of OD PMTs. One of the primary goals of the system is to inject enough light to saturate the  
85 OD PMTs. This goal drives a large part of the photon output optimisation, and Monte Carlo  
86 (MC) studies to evaluate the amount of photons required to do this are shown in Section 3.  
87 The diffuser design is discussed in Section 5. These will each be illuminated by individual  
88 LED pulser boards with 365 nm LEDs. This will require at least 122 dedicated LED pulsers,  
89 and spares should be readily available for hot-swapping should a board encounter issues. Full  
90 details of the pulser board design are given in Section 7. The pulser boards will be powered  
91 and controlled by commercially-available Field Programmable Grid Array (FPGA) boards.  
92 The control system architecture for these consists of three primary components:

- 93 • **Blade:** Interfaces directly with the FPGA, distributing all differential signals into the  
94 crate system.
- 95 • **Backplane:** Routes differential signals to the pulser boards and provides the primary  
96 power distribution, accepting 12 V and  $\pm 5$  V inputs.
- 97 • **Eurocards:** Host the pulser boards, receive power and differential signals from the  
98 backplane, and incorporate the necessary circuitry for laser triggering.

99 Further details on the control system and individual electronics crate components are given  
100 in Sections 10 and 11 respectively.

101 Light will be transported between the pulsers and diffusers by a series of fibre optic  
102 cables; following the investigations in [1] the Thorlabs FP400URT [2] is targeted for this.  
103 Due to production limitations, it is not possible to keep all fibre path lengths the same.  
104 Instead there will be five different lengths: 50 m, 80 m, 106 m, 124 m and 168 m. The  
105 light output after signal attenuation and dispersion in these fibres should be as consistent  
106 as possible, which will require fine tuning given the different amounts of attenuation and  
107 dispersion which pulses will experience based on fibre length.

108 The initial design requirements for the system are to produce pulse widths out of the  
109 diffuser of no more than 10 ns, with a photon yield in the range 1–15 million photons per  
110 pulse (ppp). The 10 ns limit is driven by the timing resolution of the WLS plates. The  
111 wavelength of light used is also partially dictated by the WLS plates, which will not activate  
112 for light above 400 nm. The photon yield target here is more of a goal than a requirement,  
113 and saturation studies were performed using numbers motivated by system performance.  
114 These are summarised in Section 3.

### 115 3 OD PMT Saturation Study

116 The light injection system in the OD will use collimated and diffuse light injection to calibrate  
117 the PMTs and to measure the optical properties (scattering and absorption) of water, as well  
118 as any degradation in Tyvek reflectivity over the course of operation.

119 Diffuse light sources will be used for in-situ calibration of the PMT charge response.  
120 Light will be injected at very low levels to measure the single-photoelectron charge response,  
121 and the requirement to achieve single-photoelectron coverage across all PMTs was used to  
122 determine the number of light injectors required for the light injection calibration system, as  
123 reported in the Outer Detector Technical Report [3]. In order to calibrate the PMTs across  
124 their entire range, the light injection system must also be capable of illuminating PMTs to  
125 saturation, to understand the change in their response as they approach saturation.

126 This section describes the use of diffuse light injection to evaluate the suitability of light  
127 sources for in-situ measurements of the PMT saturation response. Section 3.1 describes the  
128 diffuser simulation, Section 3.2 gives details of the OD geometry and diffuser parameters

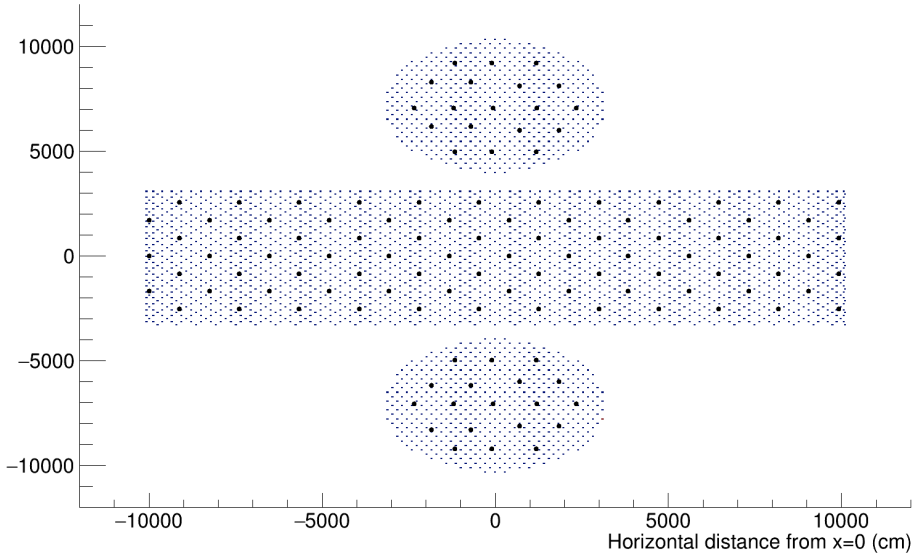


Figure 2: Positions of the OD PMTs and diffuser positions used in the calibration simulations. Note that the positions of PMTs in the top and bottom rows of the barrel have changed in the design, and as such the results presented in this tech note reflect these changes. This differs from the most recent version of WCSim (1.12.26) [4] that has been used as a basis for the simulation, and the changes are reflected in pull request #525.

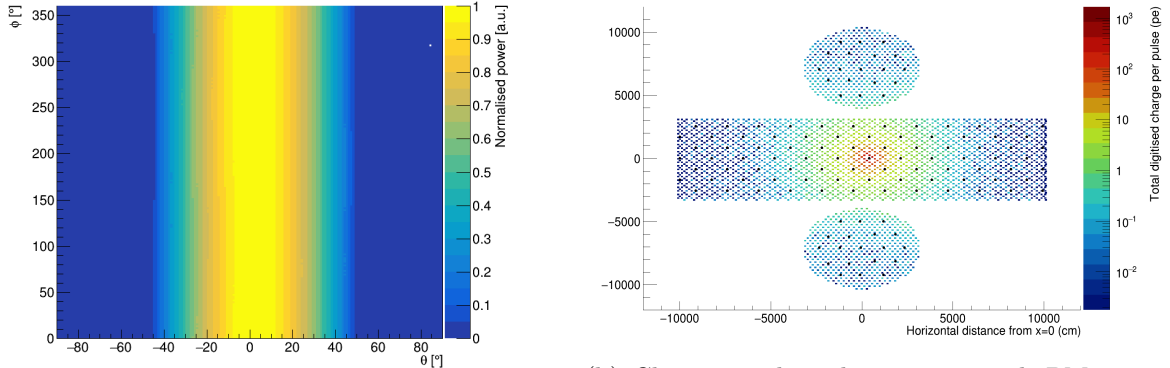
129 used, and Sections 3.3 and 3.4 describe the scope, analysis and results of the saturation  
130 study.

### 131 3.1 Diffuser Simulation

132 The planned light injection calibration system will include 122 diffusers, as determined by  
133 maximising the single-photoelectron coverage of all of the OD PMTs [3]. The division of dif-  
134 fusers between the endcaps and barrels, and their positions in terms of the overall geometry,  
135 has been altered since [3], following an update of the design and geometry in the simulation.  
136 Figure 2 shows the updated diffuse light injector (LI) locations with respect to OD PMT  
137 positions. The diffusers have been positioned as close to equidistant as possible from the  
138 surrounding PMTs, next to a strut in an empty cell.

139 A new LI generator has been written within the framework of WCSim [4]. This allows  
140 the user to define the characteristics of the LI within a data file input to the simulation. The  
141 following characteristics can be defined:

- 142 • Global position within the detector geometry,
- 143 • Direction of the LI axis,
- 144 • Wavelength of the optical photons
- 145 • Pulse width
- 146 • Photons per pulse
- 147 • LI profile in the form of arrays of  $\theta$ ,  $\phi$  and measured light intensity, where  $\theta$  is the  
148 angle made with the axis of the LI and  $\phi$  is the rotation around the axis.



(a) ID diffuser profile measured in water, used for the diffuser simulations described in this technical report. A measured profile for each diffuser will be stored in the database for OD calibration.

(b) Charge in photoelectrons on each PMT produced when the profile in (a) is used to simulate optical photons from a diffuser pointing outwards in the barrel OD. The size of the PMT + WLS plates has been increased only in the plot for improved visualisation.

Figure 3: Diffuser profile measured in water, and the resulting charge map from this profile.

The LI profile opening angle and intensity can reflect either a flat angular distribution of photons within the desired angular range of the light injector (-opening angle, +opening angle), or can be drawn from the measured profile for that injector, in which case the LI generator accurately models the variation across the profile, and in particular the drop-off in the frequency of photons towards the edge of the LI profile. For each pulse, the generator samples the specified number of photons per pulse, each with an energy calculated from the wavelength set in a database currently stored within WCSim, and a time sampled from a Gaussian distribution around the mean, with a variance equal to the pulse width specified in the database. Each photon is also assigned a global direction, which is sampled with a distribution corresponding to the LI profile.

The profile of each diffuser will be measured and stored in the database as a function of the diffuser identifier number in the final simulation. For the purposes of the diffuser simulations presented in this tech note, a single profile taken from the measurement of a diffuser profile in water has been used. This diffuser profile corresponds to an opening angle of around 40°. Since the OD diffuser profiles have not yet been measured in water, an ID diffuser profile has been used to approximate a realistic OD diffuser profile. Although the design of the OD diffusers has been modified from the ID diffuser design in order to increase the diffuser efficiency, the design has been shown to maintain the desired profile and as such the ID diffuser profile is expected to be a reasonable approximation. The diffuser profile used, and the resulting charge map from a diffuser in the barrel is shown in Figure 3.

### 3.2 Diffuser and OD Parameters

The characteristics of diffusers simulated in the saturation study are summarised in Table I. The number of photons per pulse used in the simulation was based on measurements made from the LED pulser setup, using a chain of fibre optic cables equating to 181 m in length. The simulations described here use two different values for the number of photons per pulse, corresponding to a maximum photon yield from the fibre optic chain of  $11 \times 10^6$  photons per pulse and  $20 \times 10^6$  photons per pulse. This was modified to account for an assumed diffuser efficiency of 50%. As such, the simulated numbers of photons per pulse are  $5.5 \times 10^6$  and  $10 \times 10^6$  respectively.

Parameter	Assumed value
Photons per pulse	$11 \times 10^6, 20 \times 10^6$
Wavelength	365 nm
Pulse width	10 ns
Diffuser efficiency	50%

Table I: The LI configuration used in the diffuser simulations for the saturation study presented in Section 3.3.

178 The OD geometry parameters that have been used in the simulations for the saturation  
 179 study are shown in Table II.

Parameter	Assumed value
PMT radius	8 cm
PMT dark rate	0.4 kHz
OD lateral water depth	1 m
OD height water depth	2 m
OD dead space	60 cm
Tyvek sheet thickness	1 mm
WLS plate thickness	6 mm
WLS plate length	30 cm

Table II: The OD configuration used for the saturation study presented in Section 3.3 using WCSim version 1.12.26.

180 **3.3 Saturation Analysis**

181 The limit of the PMT range is governed by the electronics response, which is expected to  
 182 fully saturate at around 100 photoelectrons (pe) in a 16 ns time window. The simulation of  
 183 the PMT charge response in WCSim does not currently fully handle the saturation, but it is  
 184 expected that the linearity of the charge response will break down between 80 pe and 100 pe.  
 185 Saturation measurements aim to measure the PMTs over the full range of this breakdown  
 186 in linearity. The saturation level for the purposes of this study has been taken to be 100 pe  
 187 in 16 ns, but the analysis has been designed to take into account the need to measure across  
 188 the entirety of this range.

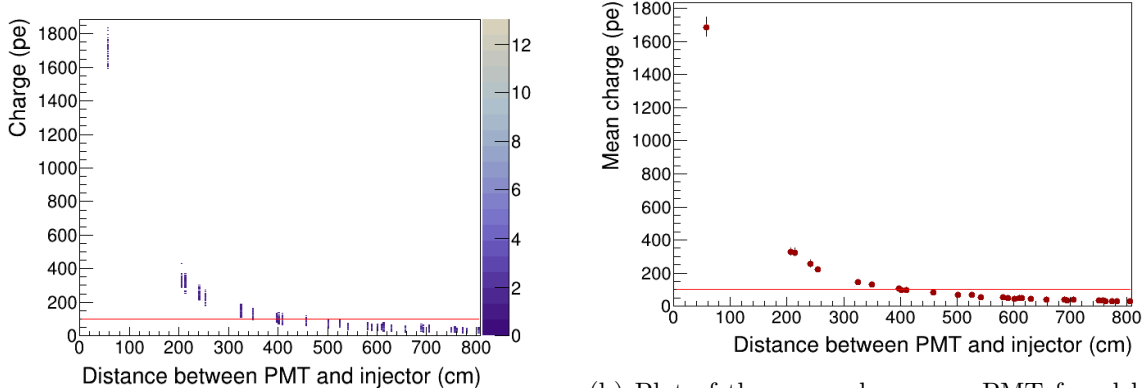
189 The saturation of OD PMTs has been evaluated in the top endcap, barrel and bottom  
 190 endcap. The diffuser simulations are intensive, requiring millions of tracked photons to  
 191 simulate a single flash, and the OD parameters are not yet finalised. As such, only two  
 192 diffusers in each of the top endcap, barrel and bottom endcap have been simulated for this  
 193 current study.

194 Two values have been used as figures of merit to determine the PMT saturation coverage:

- 195 • Mean saturation distance - the distance from the nearest diffuser at which the mean  
 196 charge per PMT is greater than saturation level.
- 197 • Saturation limit - the greatest distance from the nearest diffuser at which the charge  
 198 on any PMT reaches the saturation level.

199 For each configuration, the charge per PMT was plotted as a function of the distance  
 200 from the nearest diffuser, to give the saturation limit (Figure 4a). The mean saturation  
 201 distance was then found by taking the mean of the same plot (Figure 4b). The plot showing

202 the saturation limit is particularly useful in understanding the range of distances over which  
 203 it is possible to see the expected range of breakdown of linearity.



(a) Plot of the charge per PMT as a function of the distance from the nearest diffuser. The saturation limit is the greatest distance at which saturation is achieved i.e. 5.0 m in this case.

(b) Plot of the mean charge per PMT found by taking the mean of the left-hand plot. The mean saturation distance is the greatest distance at which the mean charge per PMT is greater than the saturation level i.e. 4.0 m.

Figure 4: Sample plots showing the mean saturation distance and saturation limit used as figures of merit for the saturation study. The red, horizontal lines mark the assumed saturation level of 100 pe.

204 Since only six diffuser locations have been simulated, the percentage of PMTs within  
 205 the mean saturation distance and saturation limit is calculated assuming symmetry both of  
 206 the detector and of the diffuser positions with respect to the PMTs. However, for practical  
 207 reasons, the diffusers have to be positioned off-centre in the empty cells between PMTs, next  
 208 to the struts on the PMT support structure. As such, a full simulation of all diffusers should  
 209 be performed in future, once the OD geometry and LI specifications have been finalised, for  
 210 an accurate evaluation of the percentage saturation across the whole detector.

### 211 3.4 Results

212 The mean saturation distance and saturation limit were evaluated for two OD diffuser loca-  
 213 tions in each of the top endcap, barrel and bottom endcap. The results for  $5.5 \times 10^6$  photons  
 214 per pulse are shown in Table III, along with the percentage of PMTs within the mean sat-  
 215 uration distance and saturation limit. Table IV shows the mean charge at the calculated  
 216 saturation distance and the mean charge at the saturation limit at the six diffuser positions.  
 The results for  $10 \times 10^6$  photons per pulse are shown in Table V and Table VI.

OD location	Mean saturation distance	% PMTs within saturation distance	Saturation limit	% PMTs within saturation limit
Barrel 1	4.0 m	31%	5.0 m	50%
Barrel 2	4.0 m	31%	5.0 m	50%
Top endcap 1	3.7 m	27%	3.9 m	30%
Top endcap 2	3.6 m	24%	4.3 m	37%
Bottom endcap 1	3.6 m	24%	4.3 m	37%
Bottom endcap 2	3.5 m	22%	6.1 m	66%

Table III: Results for PMT saturation using the diffuser configuration detailed in Table I with  $5.5 \times 10^6$  photons per pulse.

OD location	Diffuser position (cm)	Mean charge (pe) at sat. distance	Mean charge (pe) at sat. limit $\pm 2\sigma$
Barrel 1	(395.65,-3281.50,8.75)	108	$68 \pm 12$
Barrel 2	(3281.50,395.65,1705.55)	105	$67 \pm 11$
Top endcap 1	(-70.7,-97.3,3350.82)	106	$96 \pm 14$
Top endcap 2	(-707,-968.2,3350.82)	108	$77 \pm 13$
Bottom endcap 1	(-707,-968.2,-3350.82)	108	$77 \pm 14$
Bottom endcap 2	(707,-1157.8,-3350.82)	114	$42 \pm 11$

Table IV: PMT saturation levels for the figures of merit detailed in Table III with  $5.5 \times 10^6$  photons per pulse.

OD location	Mean saturation distance	% PMTs within saturation distance	Saturation limit	% PMTs within saturation limit
Barrel 1	5.4 m	57%	6.9 m	86%
Barrel 2	5.4 m	57%	6.9 m	86%
Top endcap 1	5.3 m	48%	6.3 m	69%
Top endcap 2	4.3 m	37%	6.7 m	74%
Bottom endcap 1	4.3 m	37%	6.4 m	70%
Bottom endcap 2	4.3 m	37%	6.5 m	72%

Table V: Results for PMT saturation using the diffuser configuration detailed in Table I with  $10 \times 10^6$  photons per pulse.

OD location	Diffuser position (cm)	Mean charge (pe) at sat. distance	Mean charge (pe) at sat. limit $\pm 2\sigma$
Barrel 1	(395.65,-3281.50,8.75)	102	$70 \pm 12$
Barrel 2	(3281.50,395.65,1705.55)	104	$69 \pm 12$
Top endcap 1	(-70.7,-97.3,3350.82)	102	$72 \pm 15$
Top endcap 2	(-707,-968.2,3350.82)	139	$65 \pm 13$
Bottom endcap 1	(-707,-968.2,-3350.82)	142	$70 \pm 12$
Bottom endcap 2	(707,-1157.8,-3350.82)	141	$69 \pm 11$

Table VI: PMT saturation levels for the figures of merit detailed in Table III with  $10 \times 10^6$  photons per pulse.

217  
218     Figure 5 shows the PMT charge map for the barrel 1 diffuser illuminated by  $10 \times 10^6$   
219 photons per pulse, with the saturation distance and saturation limits marked around the  
220 barrel PMTs.

221     Due to the differing geometry the mean saturation distance in the barrel (5.4 m for  
222  $10 \times 10^6$  photons per pulse) is slightly higher than in the endcaps (4.3-5.5 m), and the  
223 percentage of PMTs within the mean saturation distance in the barrel is higher at 57% than  
224 in the endcaps (37-48%). Similarly, the percentage of PMTs within the saturation limit in  
225 the barrel is higher than in the endcaps (with the exception of the bottom endcap 2 diffuser  
226 with  $5.5 \times 10^6$  photons per pulse) with 86% of barrel PMTs within the saturation limit of  
227 6.9 m. It should be noted that changes to the OD geometry, including the addition of further  
228 PMTs in the endcaps, are possible, and have not been taken into account in this simulation.  
229 Further, 100% saturation of the OD PMTs is not possible with any realistic setup, due to  
230 the large amount of required fibre and therefore attenuation, along with the geometry of the  
231 detector. Coverage obtained from this system is significantly larger than for the OD system

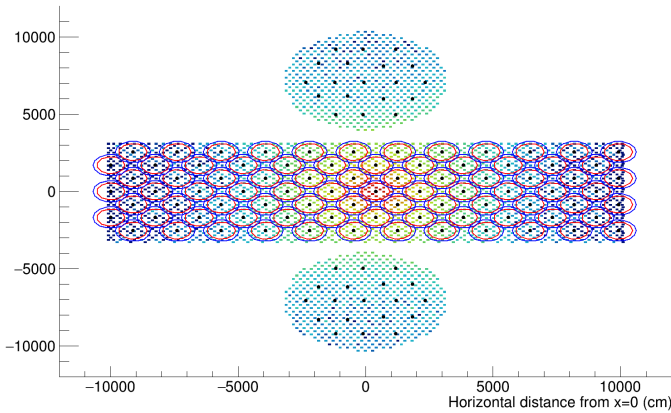


Figure 5: Charge in pe on each PMT as a result of illumination with the barrel 1 diffuser illuminated by  $10 \times 10^6$  photons per pulse. The mean saturation distance and saturation limit around each PMT in the barrel are marked in red (smaller circles) and blue (larger circles) respectively.

232 in Super-K, which was desired to improve calibration effectiveness.

233 The diffuser position with respect to the surrounding PMTs has an observable effect  
 234 on the saturation levels achieved. Where the diffuser positions with respect to surrounding  
 235 PMTs are equivalent, as in the case of the two barrel diffusers, as well as the bottom endcap  
 236 1 and top endcap 2 diffusers, saturation levels are largely the same for both light intensities.  
 237 However, the positions of the top endcap 1 and bottom endcap 2 diffuser each differ from  
 238 all other diffusers simulated, resulting in different saturation distances and saturation lim-  
 239 its. Again, a full simulation of all diffuser positions should be carried out to fully evaluate  
 240 achievable saturation across the whole detector, once all parameters and geometries have  
 241 been finalised.

## 242 4 OD Collimator Studies

243 Collimated light sources will be used to make measurements of scattering and absorption in  
 244 water, and Tyvek reflectivity. These will be used to calibrate for changes in the detector  
 245 properties over time. This will require untangling the effect of each of the properties in order  
 246 to discriminate changes in each of the properties. The first step is to evaluate the sensitivity  
 247 of collimators to changes in each of the properties separately.

248 This section presents the collimator sensitivity studies which were carried out in 2023,  
 249 prior to updates to the OD geometry and more recent updates to the light-injector simulation.  
 250 Section 4.1 describes the positioning of collimators, and the simulation method. The analysis  
 251 of sensitivity to water properties and Tyvek reflectivity are presented in Section 4.2, and the  
 252 results are presented in Section 4.3.

### 253 4.1 Collimator Simulation

254 The collimated light sources were simulated using the LI simulation described in Section 3.1.  
 255 For this collimator study, a flat profile with an opening angle of  $2^\circ$  was taken as the baseline,  
 256 and the OD configuration described in Table II in Section 3.2 was used. Figure 6 shows the  
 257 charge map produced by the  $2^\circ$  collimator source in the top endcap.

258 The sensitivity of each of the collimators to changes in absorption, Rayleigh scattering

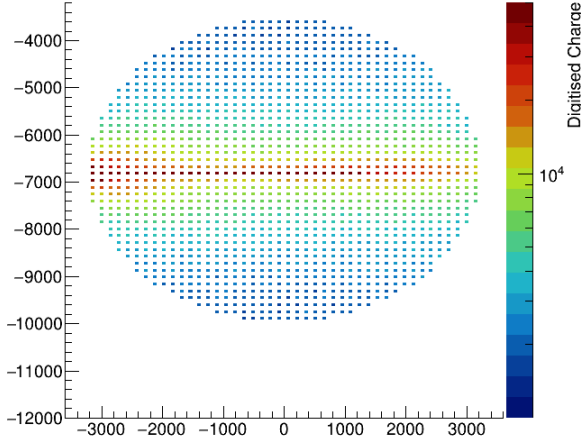


Figure 6: Distribution of charge collected in end cap PMTs for a collimated beam of light injected from the right hand side, travelling across the diameter of the OD to the left hand side.

and Tyvek reflectivity was evaluated by varying each property one at a time, scanning over values up to 30% either side of the nominal value for absorption and scattering, and 30% lower than the expected value for Tyvek reflectivity. Nominal values have been extrapolated from Super-Kamiokande measured values in the case of scattering and absorption, and from the expected value in the case of the Tyvek reflectivity. These values and the range of the scans over each property are shown in Figure 7.

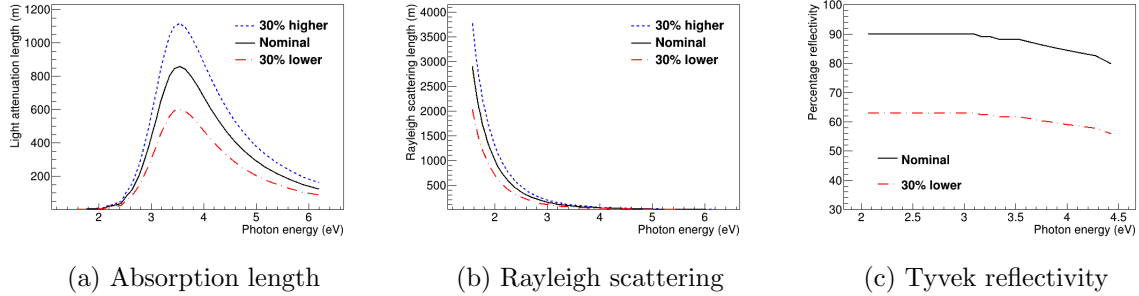


Figure 7: Nominal (black, solid), maximum (blue, dashed) and minimum (red, dot-dashed) values for the scans over absorption length and Rayleigh scattering, and nominal (black, solid) and minimum (red, dot-dashed) values for the scans over Tyvek reflectivity.

Variable steps were chosen for the scan over the range for each property to allow sufficiently detailed evaluation of the sensitivity to changes in each property. For absorption and scattering, the parameters are varied in steps of 1% between  $\pm 5\%$ , where finer binning is required to see the small effects at these variations. From 5% to 30% either side of the nominal, the parameters were varied in 5% steps. For Tyvek reflectivity, the parameter is reduced by up to 30% either side of the nominal, in 0.5% steps up to  $\pm 5\%$ , 1% steps between  $\pm 5\%$  and  $\pm 10\%$  and in 5% steps above that.

The scans over the variation in parameters require at least 21 individual simulations per property, and each simulation requires  $\mathcal{O}(100M)$  photons to produce sufficient statistics. In addition, the OD geometry remains in flux. As such, although the OD light injection system will include 12 OD collimators, a single collimator in each of the OD top endcap, barrel and

bottom endcap was simulated for the purposes of these studies.

## 4.2 Collimator Sensitivity Analysis

To evaluate the sensitivity of the collimator to each of the parameters, the distribution of charged collected in the PMTs as a function of the distance from the light injector was compared over the scan ranges detailed in Section 4.1. These were compared using a Pearson's  $\chi^2$  test:

$$\chi^2 = \sum_{s=0}^S \frac{(O_s - E_s)^2}{E_s}, \quad (1)$$

where the expected value  $E_s$  is the charge on the PMTs at distance  $s$  for the nominal parameter value, and the observed value  $O_s$  is the charge on the PMTs at distance  $s$  for the varied parameter value. In this way, the distribution of  $\chi^2$  values as a function of the percentage change in parameter value indicates the sensitivity of the collimator to the changes in each of the properties. For this analysis, only PMTs located in the same part of the detector as the collimator were included in the  $\chi^2$  calculation.

Errors on the  $\chi^2$  statistic were calculated by splitting the sample into 10 sub-samples, calculating the Pearson's  $\chi^2$  test statistic for each sub-sample and then calculating a relative standard deviation from the variance between the sub-samples.

## 4.3 Results

Figure 8 shows the  $\chi^2/\text{ndof}$  values over the scan ranges for each of the properties investigated for a 2° collimator located at the bottom of the OD and pointing upwards in the OD barrel. The collimator is most sensitive to changes in reflectivity, and least sensitive to changes in absorption. The results for the barrel collimator shown in Figure 8 indicate that for this collimator configuration, sensitivity at the 99% confidence level can be achieved for changes in reflectivity at the sub-percent level, a reduction in the absorption length of 20% can be detected at the 95% confidence level and a change in the scattering length can be detected at the 99% confidence level within a few per cent of the nominal value.

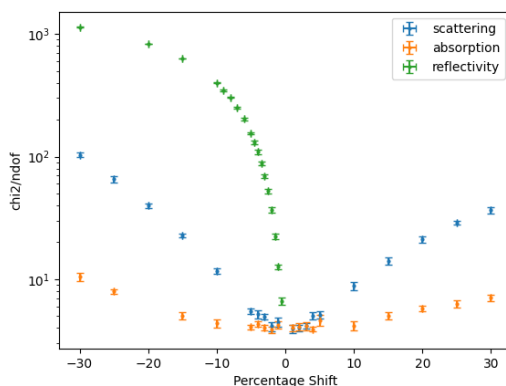


Figure 8: Change in  $\chi^2$  statistic with variation in absorption (orange), Rayleigh scattering (blue) and Tyvek reflectivity (green) up to 30% from the nominal value.

For the baseline analysis, the collimator has been positioned close to the front face of the PMTs. However, the location of the collimator, in terms of distance from the front face of the PMTs, can affect the sensitivity to changes in the parameters, particularly in the case of reflectivity, as shown in Figure 9. Ultimately the positioning of the collimator will

be constrained by practical considerations and, as such, the sensitivity of the collimators to absorption, scattering and Tyvek reflectivity should be reassessed once the OD geometry and collimator positioning have been finalised.

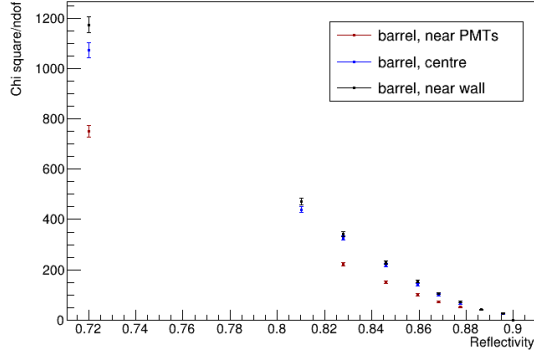


Figure 9: Change in  $\chi^2$  statistic with variation in Tyvek reflectivity up to 30% from the nominal value for a collimator positioned close to the PMTs (red), halfway between the PMTs and tank wall (blue), and close to the tank wall (black).

The collimators have been designed to be tunable to different open angles. A comparison of the results for a  $2^\circ$  and  $1.35^\circ$  collimator in the same position in the barrel is shown in Figure 10. With a straight comparison of the Pearson's  $\chi^2$  test statistic for the two collimators, there was no obvious change in the sensitivity to changes in any of the parameters. However, a more detailed analysis which takes into account additional information, such as the timing of the PMT hits as a function of PMT location, should be performed to re-evaluate the effect of the opening angle on collimator sensitivity to each of the properties investigated.

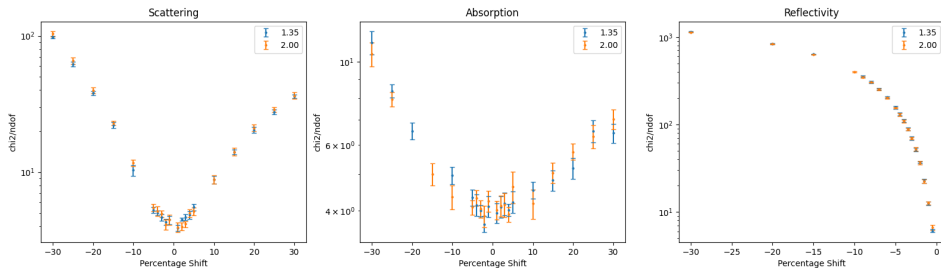


Figure 10: Change in  $\chi^2$  statistic with variation in Rayleigh scattering (left), absorption (centre) and Tyvek reflectivity (right) up to 30% from the nominal value for a  $2^\circ$  collimator (orange) and  $1.35^\circ$  collimator (blue).

These results represent a preliminary evaluation of the sensitivity of the OD collimator system to the three properties investigated, and presents the first step in the development of an analysis to measure these properties using the collimator system. This will rely on discriminating the effect of changes in each property simultaneously and will require a more complex analysis. This analysis should be performed once the OD geometry has been finalised.

316 **5 Diffuser Design**

317 **5.1 ID Diffuser Hemisphere Design**

318 **5.1.1 Inner Detector Diffuser Design**

319 The diffusers used to scatter input laser light in the inner detector volume are 2.54 cm  
320 half-spheres fabricated from PTFE. This is used as it

- 321 • is unaffected by immersion in water  
322 • acts as a excellent diffuser  
323 • is a good transmitter of UV light  
324 • is easy to machine and clean

325 A mechanical drawing of the inner detector diffuser hemispheres is shown in Figure 11

326 **5.1.2 Diffuser Profile Measurement System**

327 A scanning system was built to measure the output characteristics of diffuser hemispheres.  
328 Enclosed in a dark box, the diffuser is mounted onto two rotary stages which gives the freedom  
329 to rotate the diffuser around the nominal axis linking the diffuser with the photosensor. This  
330 scanner only takes scans in an air medium, and the setup is illustrated in Figure 12.

331 A laser powered from a wall plug is used to illuminate the diffuser with light at a wave-  
332 length of 450 nm. It is triggered by a function generator with 1000 triggers per burst at a  
333 frequency of 2 kHz. The open beam is directed via a mirror, a circulator, and a lens to the  
334 fibre launch stage, and then via an optical fibre towards the diffuser. The diffuser enclosure is  
335 fixed with three screws on the double-rotation stage. Measurements of bare diffuser profiles,  
336 i.e. without enclosure, are conducted with the bare fibre end positioned in the centre of the  
337 rotation stage using a 3D printed frame. The bare fibre end is kept in place due to friction  
338 on the connection point with the diffuser hemisphere. A photograph of the rotation stage  
339 with a bare diffuser hemisphere is shown in Figure 13.

340 A PMT measures the diffuser spectrum at a fixed position, with 62 cm distance to the  
341 diffuser enclosure and a 3 mm pinhole aperture, restricting the solid angle viewed by the PMT  
342 to  $2 \cdot 10^{-5}$  sr. For comparison, a single 50 cm PMT in the HK far detector receives light from  
343 a point source at the other side of the tank over a solid angle of approximately  $2.2 \cdot 10^{-4}$  sr.  
344 The PMT signal is digitised at a sampling rate of 2500 MHz over 1000 cycles, allowing to  
345 resolve the shape of each single signal waveform. The light yield at each coordinate is then  
346 obtained as the average waveform area across all digitised signals.

347 The diffuser profile measurement system is discussed in detail in [5].

348 **5.1.3 Diffuser Power Measurement System**

349 In addition to the profile measurement functionality, the integrated power output from the  
350 diffuser was measured using an integrating sphere from Ophir. This sphere provides an  
351 unbiased measurement of the total light output power of any light source, regardless of the  
352 shape of the emission profile. A bespoke diffuser holder suitable for connection to one of the  
353 integrating sphere ports was 3D-printed, as was a holder for the optical fibre from the laser  
354 source.

355 A bare PTFE hemisphere was mounted into this holder and connected into the integrating  
356 sphere port. The bare end is inserted into the connection point in the same manner as for  
357 a bare profile scan. Tape was used to in order to prevent light leaking out of the back

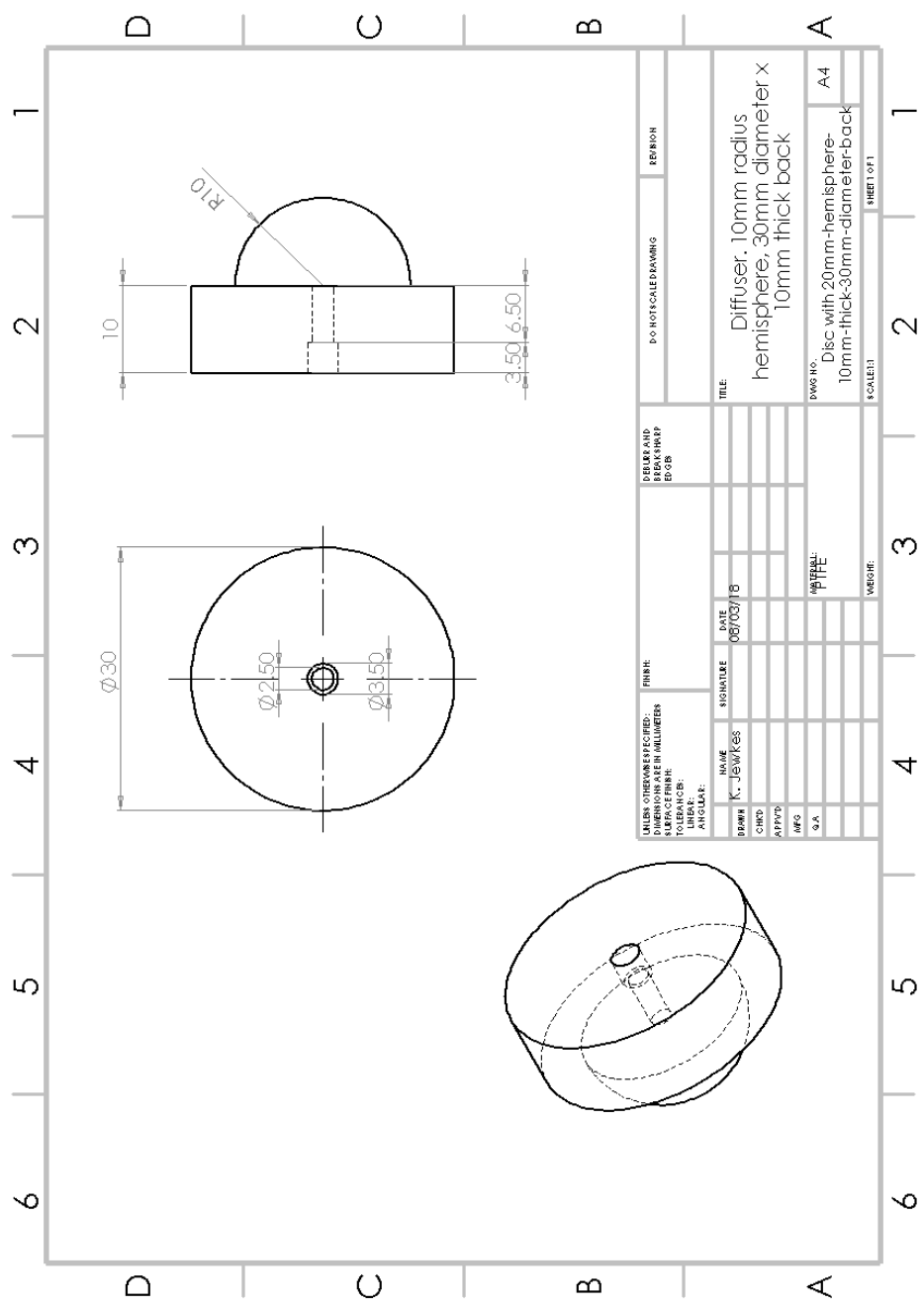


Figure 11: Bare Diffuser Mechanical Drawing

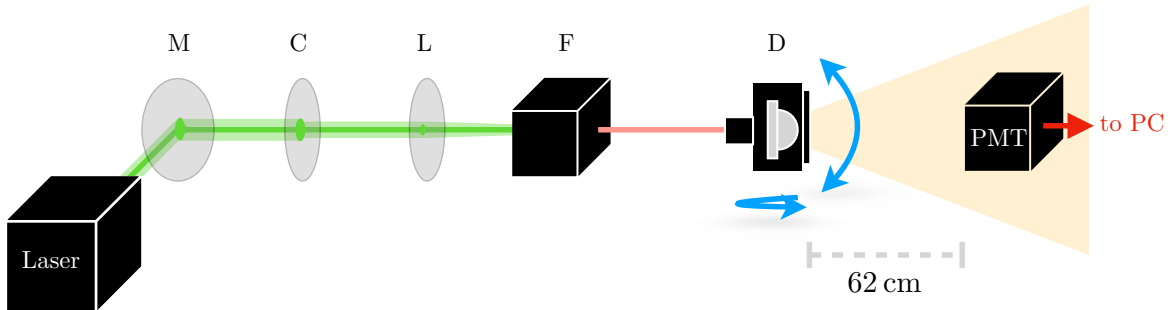


Figure 12: Setup for diffuser scans: light from the laser is directed via a mirror (M), a circulator (C), and a lens (L) to the fibre launch stage (F). From there, the light goes via an optical fibre to the diffuser (D) on the rotation stage.

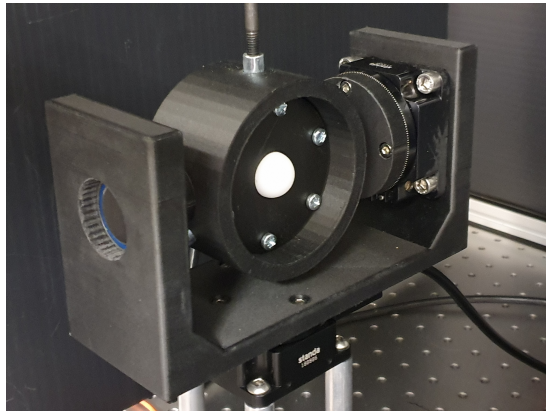


Figure 13: Rotation stage with bare diffuser hemisphere mounted using a 3D-printed frame.

of the hemisphere during the measurement, which also helped to keep the fibre in place. The hemisphere was then illuminated with light from the same laser, this time running on a continuous rather than burst setting. On the continuous setting light is supplied in a sinusoidal manner at a frequency of 1 kHz. Power measurements were taken once per second for a period of ten seconds to account for small fluctuations in laser intensity, the mean of which served as the final power measurement for that hemisphere.

In order to calculate a power ratio, a measurement of power for the bare fibre also needed to be obtained. This was done in a similar manner to a power measurement for a hemisphere, using the same laser and data acquisition settings. To make the comparison between fibre and hemisphere measurement as accurate as possible, a special hemisphere was created with the fibre connection point extended into a hole that runs through the length of the hemisphere. The bare fibre can then be inserted all the way through until it pokes out of the front, allowing a power measurement for the bare fibre to be taken with the conditions inside the integrating sphere as close as possible to hemisphere measurements. The ratio of hemisphere power to fibre power can then be taken to determine the amount of light lost.

A table of systematics for the power ratio measurement is shown in Table VII. Rotation refers to changing the orientation at which the diffuser is placed into the holder, and diffuser re-insertion refers to removing the diffuser from the holder and replacing it. Fibre re-insertions refers to disconnecting and re-connecting the fibre into the diffuser, while bare fibre refers to dis- and re-connecting the fibre when taking bare fibre measurements. This results in a total systematic of 5.3% for a diffuser measurement and 1.8% for a fibre measurement, and therefore an uncertainty of 5.6% in a power ratio measurement.

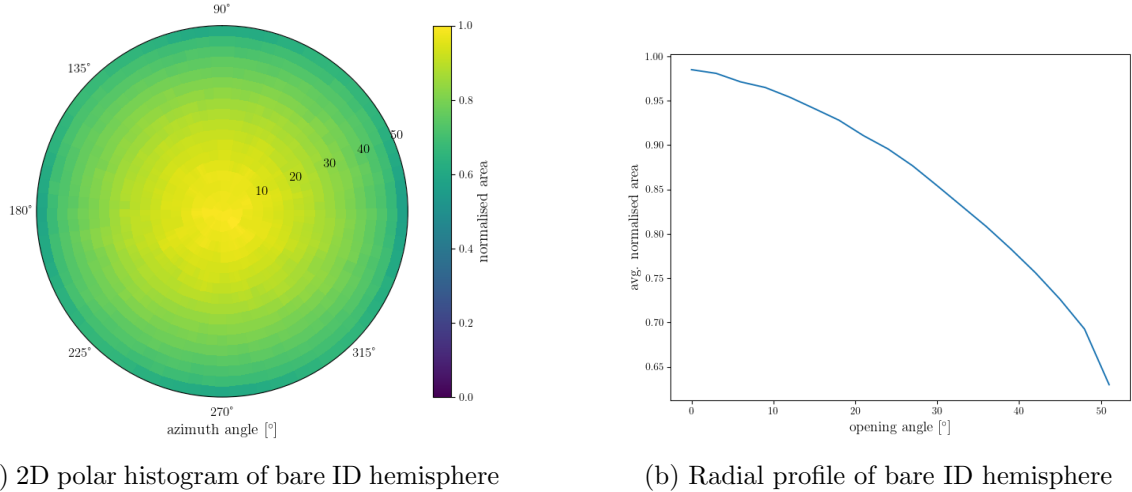


Figure 14: Profile scan of a standard bare ID diffuser hemisphere

Systematic	Std. dev. (%)
Rotation	1.4
Diffuser re-insertion	1.0
Fibre re-insertion	5.0
Bare fibre re-insertion	1.8

Table VII: Integrating sphere systematics for the power ratio measurement.

## 380 5.2 OD Diffuser Design

381 The original intention was to use the same diffuser hemisphere design for the OD diffusers  
 382 as will be used for the ID diffusers. However, the standard diffuser emits less than 20% of  
 383 the power delivered by an optical fibre. As there are a number of interfaces in the optical  
 384 pathway between the light source and the diffuser, and as the light source for the OD will  
 385 be LEDs, this was considered too low to be able to effectively saturate PMTs in the OD  
 386 space, which is one of the primary design requirements of the system. Neither the number of  
 387 interfaces in the optical chain, nor the light source can be changed easily, but it is possible  
 388 that an alternate design of the diffuser hemisphere could yield more light.

389 Light is lost to two mechanisms in the standard diffuser; absorption by the PTFE and



Figure 15: A prototype of the OD diffuser with a 2 mm top hat.

390 backscattering. Both loss mechanisms would be minimised if there were less PTFE in the  
 391 light path. The design for the OD diffuser section was modified to be the shape of a top  
 392 hat, as shown in Figure 15. The optimal depth was studied by taking profile and power  
 393 ratio measurements using the same diffuser, but at smaller and smaller depths; after each  
 394 measurement was completed, 2.0 mm was cut from the top-hat, and the measurements were  
 395 re-taken. This procedure was repeated until the top-hat was 2.0 mm high.

Top-hat depth (mm)	Power ratio (%)
10.0	19.2
8.0	32.4
6.0	31.5
4.0	42.1
2.0	55.2

Table VIII: Power ratio measurements for each depth of the top-hat

396 Results of the power ratio measurements are shown in Table VIII. As expected, power  
 397 ratio increases with decreasing top-hat depth, making the optimum depth 2.0 mm. The  
 398 profile as shown in Figure 16 confirms that the shape of the profile is still suitable.

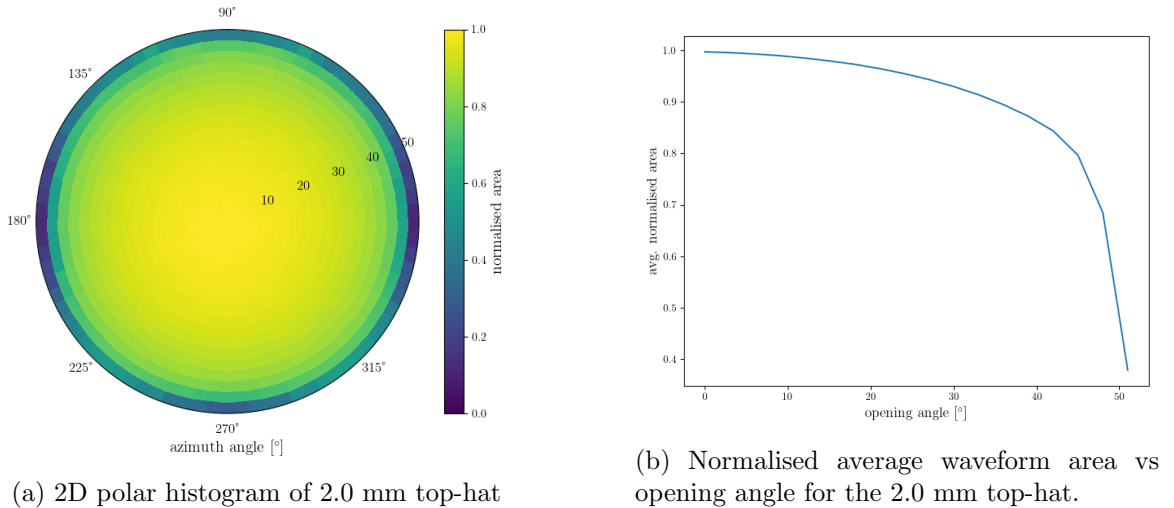


Figure 16: Profile scan of the 2.0 mm top-hat

399 Based on these studies, we propose to change the OD diffuser design from a hemisphere  
 400 to a top-hat with a 2.0 mm height above the base. The diffuser will still be fabricated from  
 401 PTFE, but this new design (i) emits more light at higher emission angles (ii) doubles the  
 402 amount of light that is emitted for a given LED power setting and (iii) is significantly easier  
 403 to fabricate in bulk.

## 404 6 OD Diffuser Mounting System and Installation

405 The OD space will be illuminated by a total of 122 OD diffusers, 19 on each of the top and  
 406 bottom caps, and 84 in the barrel. The barrel diffusers are distributed in 7 vertical layers  
 407 each consisting of 12 OD diffusers. Due to the numbers and cost, the mounting system must  
 408 be relatively small, easy to fabricate and easy to install. Installation will be carried out by  
 409 workers on the gondola in the OD space after the Tyvek has been installed and as the fibres  
 410 are being installed. The gondola worker will install the fibre in the OD diffuser, and fix the



Figure 17: (left) Front view of the prototype of the OD diffuser mount and (right) rear view of the prototype of the OD diffuser mount.

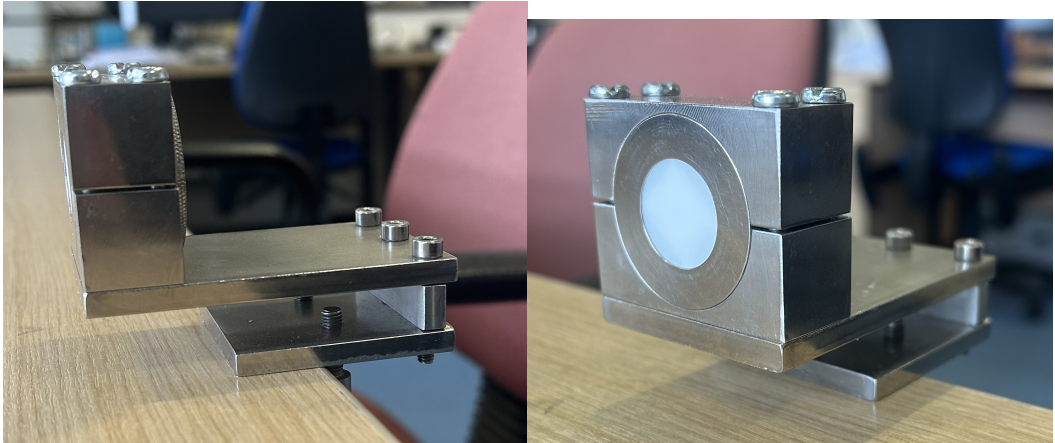


Figure 18: (left) Side view of the prototype holder and (right) front view of the prototype holder.

411 mount to the HK frame, oriented into the OD space. Since this is being done on the gondola,  
412 the mount needs to be small, easy to store, and straightforward to install.

413 Drawings for the OD diffuser prototype mount can be seen in Figure 17 and pictures  
414 of the prototype can be seen in Figure 18. The mount is made from stainless steel and is  
415 designed to hook over a horizontal frame bar, and screw in from the bottom. The PTFE  
416 mount is approximately 5 cm on a side. The fibre will be installed from the back and is held  
417 in place by a T-shaped component that is screwed down by the gondola worker. An image of  
418 the prototype housing installed on the PMT support structure mockup next to a mechanical  
419 OD PMT and WLS plate is given in Figure 19.

## 420 7 Pulser Board

### 421 7.1 Pulser Board Overview

422 The pulser board was designed to be a more efficient and compact version compared to  
423 Super-Kamiokande UK Light Injection system, improving on efficiency, functionality, and  
424 light output. The pulser board is a rather simple board designed for low cost production.  
425 This section explains each circuit, component selection and design decision. Minor changes  
426 are expected from the current design, mostly centred on removing prototyping circuitry.  
427 More details on the expected changes are given in Section 7.10.



Figure 19: OD diffuser housing installed at the RAL mockup frame, next to an OD PMT and WLS plate.

## 428 7.2 Physical Dimensions and Construction

429 The dimensions of the Printed Circuit Board (PCB) were selected to be as compact as practicable, while still providing sufficient area for the secure mounting of a fibre coupler and for  
 430 the components. The final board size is 50 mm × 30 mm. This configuration permits electrically noisy components, such as switching power supplies and the Low Voltage Differential  
 431 Signal to Transistor Transistor Logic (LVDS-to-TTL) converter to be positioned at a maximum  
 432 distance from the switching circuitry, thereby minimising potential electromagnetic  
 433 interference.  
 434

435 Although it is technically feasible to further reduce the board size, preliminary design  
 436 studies and practical build indicated no substantial benefit in doing so. The board density  
 437 cannot be significantly increased inside the crate due to FPGA LVDS count and Eurocard  
 438 dimension, and cost analyses revealed negligible differences associated with a smaller PCB  
 439 footprint. Furthermore, the chosen dimensions provide an adequate area for the fibre coupler  
 440 and the necessary mounting holes to affix the pulser board onto the Eurocard, thereby  
 441 ensuring reliable optical alignment and mechanical stability. The PCB is fabricated as a four-  
 442 layer FR4 [6] board with a thickness of 0.8 mm, in accordance with the standard construction  
 443 offered by PCB Train/Newbury Electronics<sup>1</sup>, see Figure 20. Refer to Figure 21 for the 3D  
 444 model of the pulser board. The Top Layer and Inner Top Layer are shown in Figure 22, and  
 445 the Inner Bottom Layer and Bottom Layer are likewise illustrated in Figure 23. A combined  
 446 view of all PCB layers is provided in Figure 24.

---

<sup>1</sup>These are trading names of the same manufacturer.

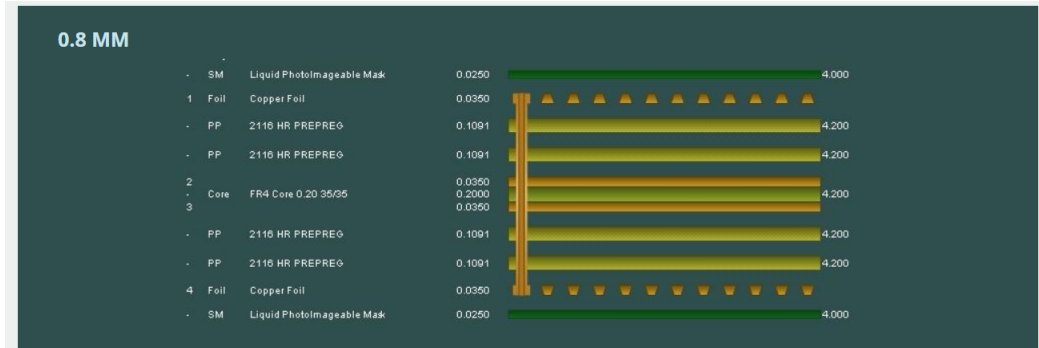


Figure 20: PCB Train's 4 Layer 0.8mm Layer Stack

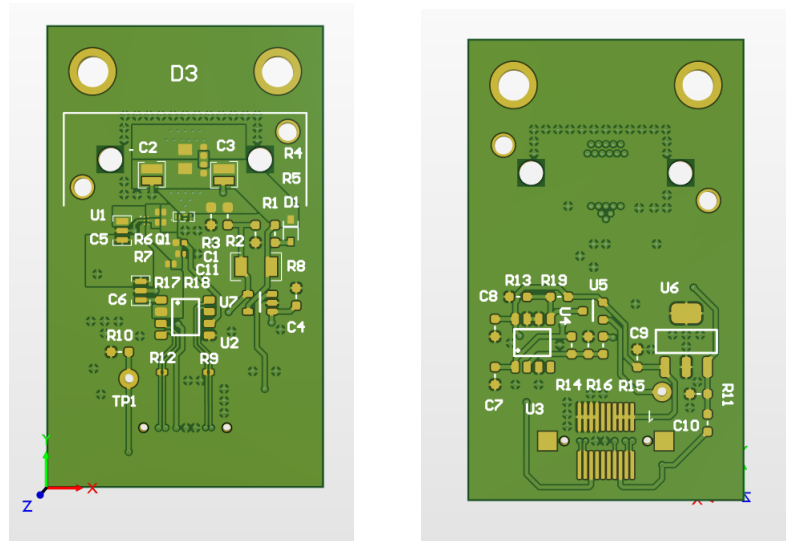


Figure 21: Pulser Board's 3D view Top and Bottom

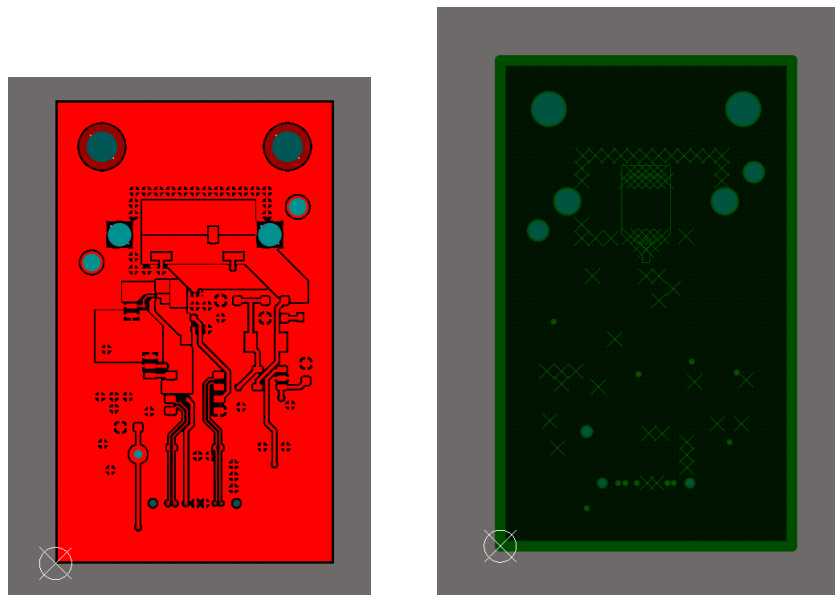


Figure 22: Pulser Board Top and Inner Top Layer

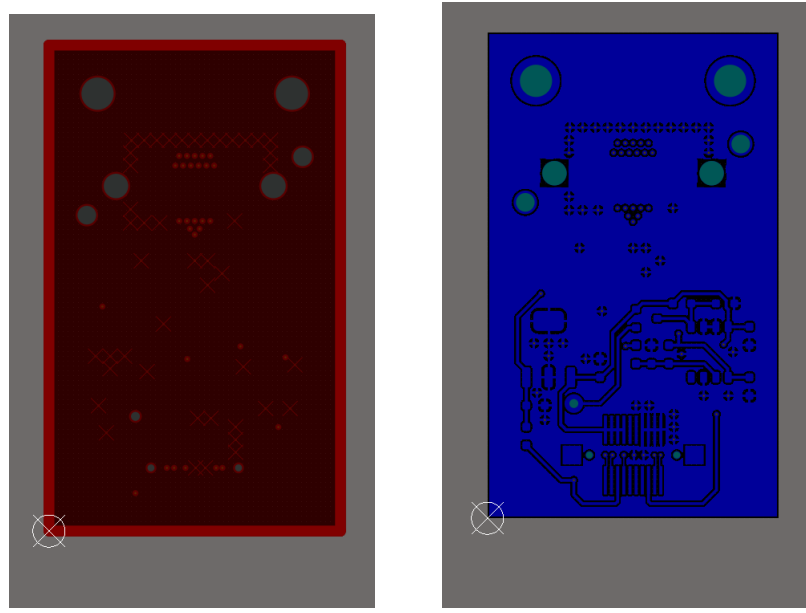


Figure 23: Pulser Board Inner Bottom and Bottom Layer

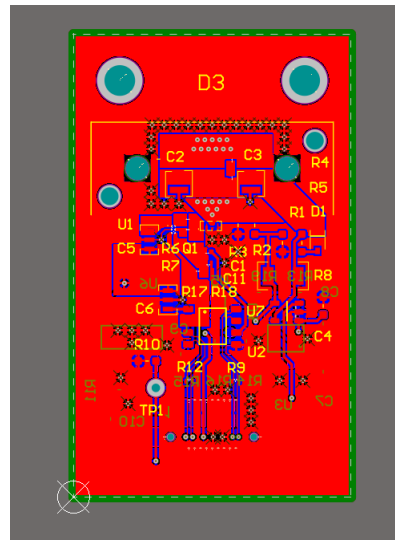


Figure 24: Pulser Board Layer Overview

448 7.3 LED

449 7.3.1 Overview

The LEDs are the most crucial component in the system as the characteristics of these primarily determine the light output, regardless of electronics. LEDs are usually not rated for such high-speed applications, which meant LEDs had to be tested and validated in-house, as datasheets do not provide the required information. The specification required was a 1–10 ns clean single pulse, sub-400 nm wavelength, small surface mount package, narrow output beam so it can be coupled to a fibre with reduced losses and a good range of photon output. Several LED packages were purchased from Kingbright and LC-LED, and their performance tested. The results of these tests are given in Section 7.3.4.

### 458 7.3.2 Switching Circuit

459 The redesign process provided a valuable opportunity to evaluate a revised layout and new  
460 components for the switching circuit. Several enhancements have since been implemented  
461 in the revised switching circuit. Most importantly, the switching side of the layout has  
462 been rerouted. In contrast to the previous configuration, where current would flow through  
463 the limiting resistor regardless of the LED state, the updated design only allows current  
464 flow when the LED is active (refer to Figure 25). This modification reduces both thermal  
465 dissipation and the overall power consumption of the system. To modulate light intensity,  
466 a variable power supply is now employed to adjust the voltage supplied to the LED. This  
467 method has proven highly effective. Tests were conducted at various voltage levels using  
468 the full 181 m length of optical fibre—the maximum expected in Hyper-K at the time of  
469 testing—and the resulting photon output ranged from approximately  $1 \times 10^5$  to  $2 \times 10^7$   
470 photons per pulse. Refined testing results are shown in Section 7.3.4. Further discussion  
471 regarding the implementation and performance of the variable voltage supply is provided in  
472 Section 7.5.

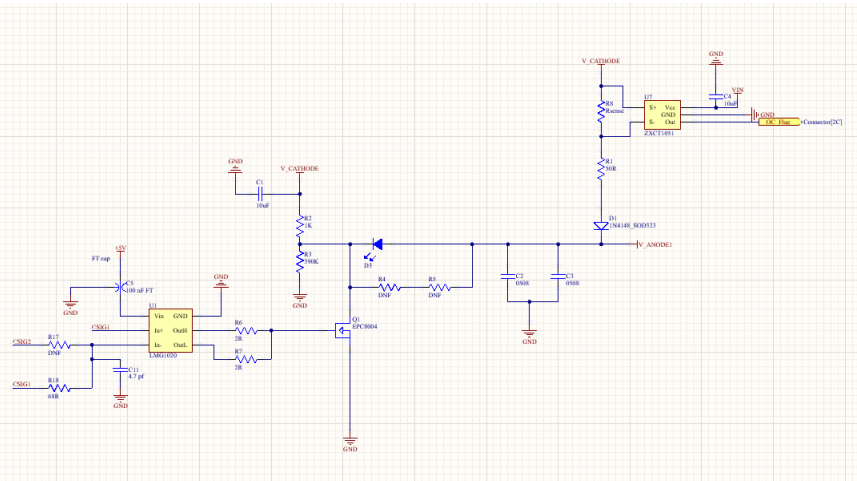


Figure 25: Switching Circuit Layout with LMG1020 and over current IC, R4 is 6.8 nH inductor and R5 is 3R3 resistor

473 7.3.3 Switch Selection

474 The previous iteration of the pulser board utilised a BFR92 [7] high-speed RF NPN switching  
 475 transistor which was directly driven by a LVDS-to-TTL converter. In the redesign phase,

476 alternative circuit topologies were explored—particularly those suitable for generating (sub-  
477 )nanosecond pulses. This investigation led to the adoption of gate driver circuits. Gate  
478 drivers are advantageous not only because they can power switches with challenging drive  
479 requirements, but also because sub-nanosecond electrical pulses can be achieved by modu-  
480 lating the enable pin with slight timing offsets.

481 The fastest commercially available gate driver identified was the Texas Instruments  
482 LMG1020 [8]. This device supports pulse widths down to 1 ns, with typical rise and fall  
483 times of 400 ps. Additionally, it features an enable pin that allows for precise nanosecond  
484 pulse shaping <sup>2</sup>. The LMG1020 is compatible with both Gallium Nitride Field Effect Tran-  
485 sistor (GaN) and Metal Oxide Semiconductor Field Effect Transistor (MOSFET) switches,  
486 broadening the scope for future component integration and experimentation. It is widely  
487 available and priced at £1.97 per unit in the quantities we will require for full production.

488 For the switching element, enhancement-mode GaN transistors manufactured by EPC  
489 were selected due to their superior switching characteristics. This recommendation origi-  
490 nated from Nick Braam, an engineer at the University of Victoria, who contributed to the  
491 pulser board design for the mPMT system [9]. Two EPC devices were shortlisted: the  
492 EPC2012 [10] and EPC8004 [11]. The EPC2012 offers a simpler footprint, which could re-  
493 duce manufacturing defects. However, the EPC8004 features lower parasitic capacitance,  
494 see Figure 26 for the EPC2012 values and Figure 27 for EPC8004 values, leading to better  
495 high-speed performance.

496 To evaluate optical output performance, a 40 m length of FP400URT [2] optical fibre,  
497 a Mouser-sourced 385 nm LED (ATS2012UV385 [12]), and a Hamamatsu H10721-210 [13]  
498 PMT were used. The EPC-based configurations exhibited nearly identical pulse shapes,  
499 whereas the BFR92-based circuit’s pulse shape was less sharp at identical pulse widths, as  
500 shown in Figure 28. Consequently, the EPC8004 (Figure 29) was chosen for implementation.  
501 Optimal performance of the EPC GaN switches required careful layout considerations. A  
502 layout was developed in accordance with EPC’s design guidelines [14], targeting minimal  
503 parasitic inductance and capacitance. The design employs two layers placed directly above  
504 one another, utilising large copper planes and multiple vias to ensure uniform current dis-  
505 tribution. The PCB will be fabricated and assembled by PCB Train, using their 0.8 mm  
506 thick, four-layer stack-up, which offers minimal inter-layer separation for optimal electrical  
507 performance (Figure 20). This same layout strategy was applied to the BFR92 circuit to  
508 provide a fair performance comparison.

509 A significant challenge at low pulse widths is the presence of a trailing edge or “tail” in  
510 the LED output. This effect arises due to charge accumulation and the intrinsic capacitance  
511 of the LED, resulting in extended decay times and pulse broadening (see Figure 30). To  
512 mitigate this, a parallel modified snubber circuit was implemented, consisting of a 6.8 nH  
513 inductor and a 3.3 Ω current-limiting resistor. Upon LED turn-off, the inductor generates an  
514 electromotive force (EMF) that actively extracts residual charge from the LED, accelerating  
515 its shutdown. The effectiveness of this approach is illustrated in Figure 31. Additionally,  
516 two 0508 reverse-topology 100 nF capacitors have been incorporated. Their role is to act as  
517 local energy reservoirs, providing rapid current delivery to the LED during pulse operation,  
518 surpassing the response time of the main power supply.

### 519 7.3.4 Testing

520 For testing purposes, the previous-generation United Kingdom Light Injection (UKLI) moth-  
521 erboard and associated software were utilised in conjunction with a prototype of the next-  
522 generation pulser board. This prototype consisted of four distinct circuit variants: one

---

<sup>2</sup>See page 12 and 13 in [8].

eGaN® FET DATASHEET			EPC2012			
PARAMETER	TEST CONDITIONS	MIN	TYP	MAX	UNIT	
<b>Dynamic Characteristics</b> ( $T_j = 25^\circ\text{C}$ unless otherwise stated)						
$C_{iss}$	Input Capacitance	$V_{DS} = 100\text{ V}, V_{GS} = 0\text{ V}$		128	145	pF
$C_{oss}$	Output Capacitance			73	95	
$C_{rss}$	Reverse Transfer Capacitance			3.3	4.4	

Figure 26: EPC2012 Capacitance Values IC

eGaN® FET DATASHEET	EPC8004
Dynamic Characteristics <sup>1</sup> ( $T_j = 25^\circ\text{C}$ unless otherwise stated)	
PARAMETER	TEST CONDITIONS
$C_{iss}$	Input Capacitance
$C_{oss}$	Output Capacitance
$C_{rss}$	Reverse Transfer Capacitance
	$V_{GS} = 0\text{ V}, V_{DS} = 20\text{ V}$
	MIN
	TYP
	MAX
	UNIT
$C_{iss}$	45
$C_{oss}$	23
$C_{rss}$	0.8
	52
	34
	1.3
	pF

Figure 27: EPC8004 Capacitance Values IC

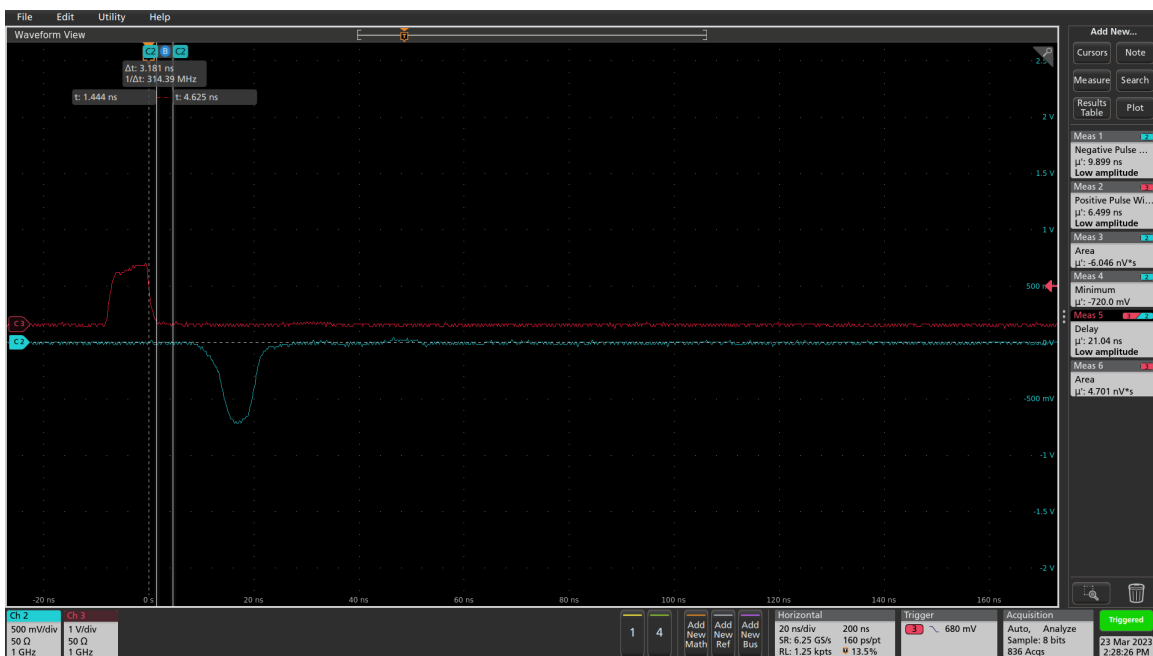


Figure 28: BFR92 Pulse Shape

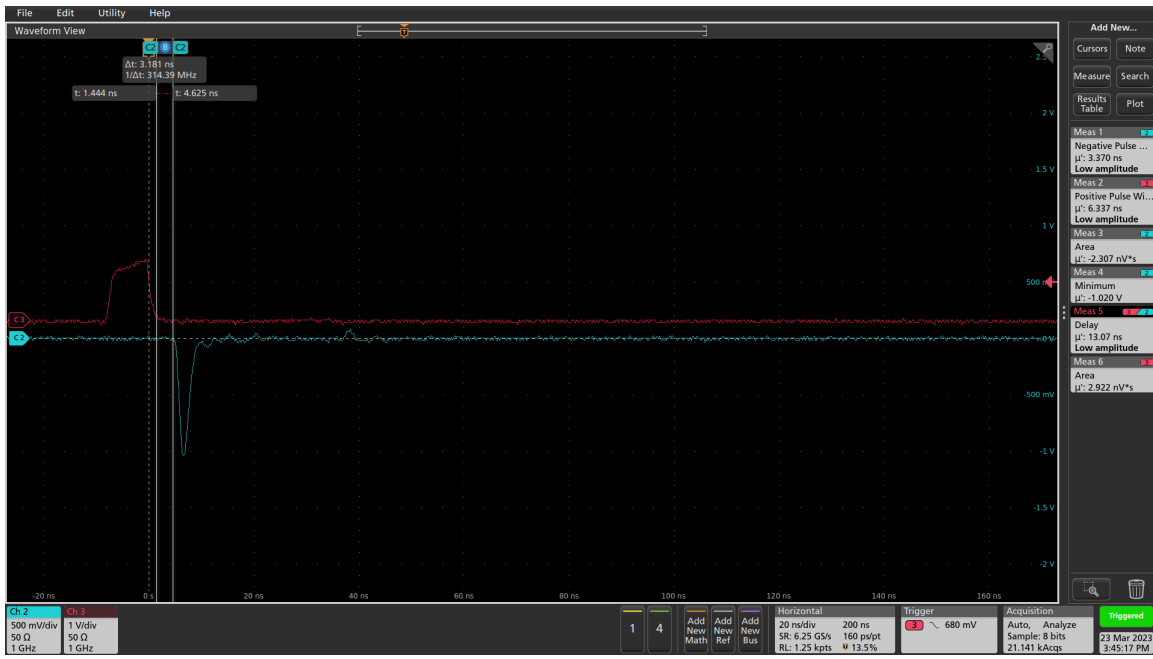


Figure 29: EPC8004 Pulse Shape

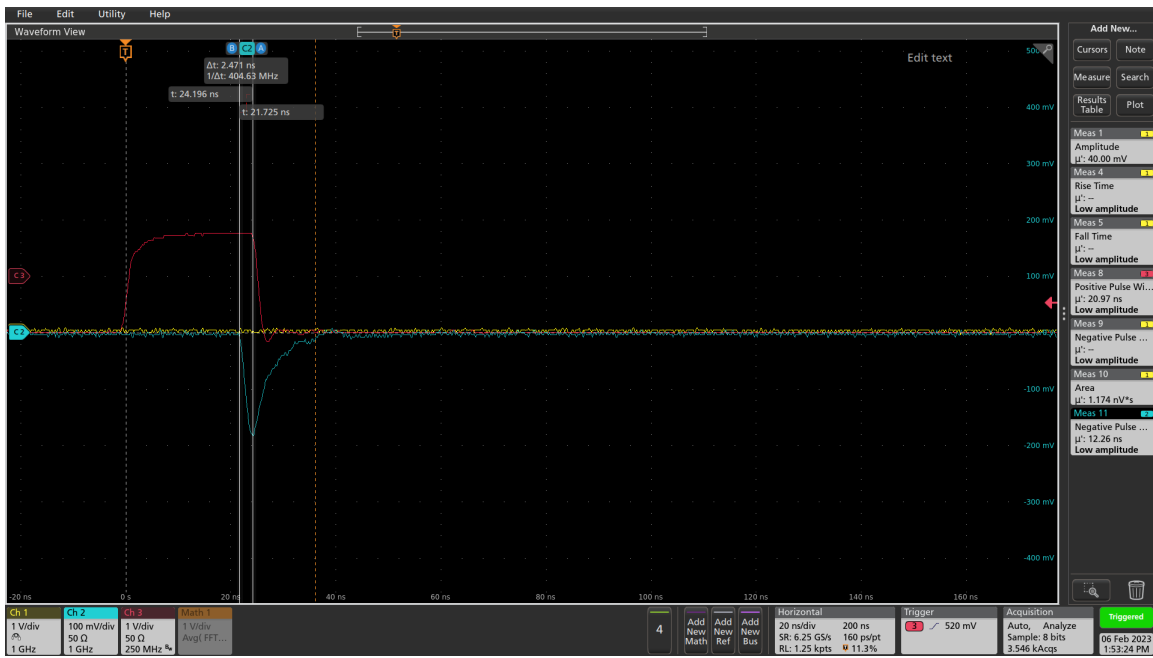


Figure 30: Pulsing Circuit With No Inductor and Resistor

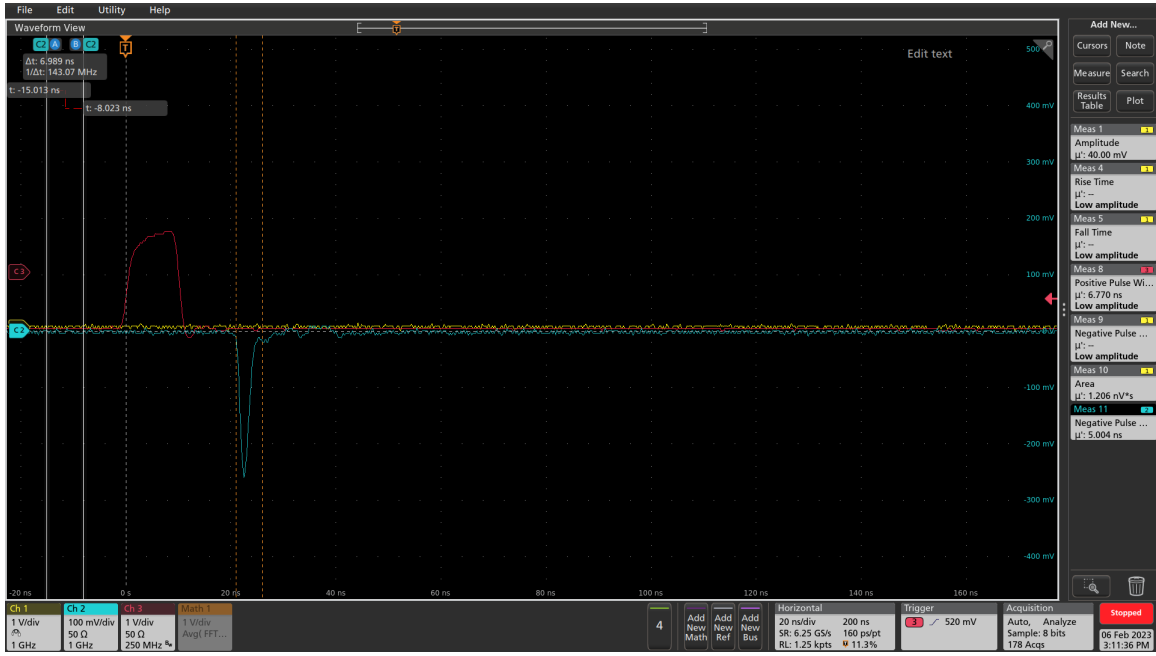


Figure 31: Pulsing Circuit With Inductor and Resistor

523 employing the EPC8004 switch, another utilising the EPC2012 switch, a third using the  
 524 same high-speed transistor (BFR92) as implemented in the legacy system, and a fourth vari-  
 525 ant incorporating an EPC2012 gate in a through-hole package instead of the standard 0805  
 526 surface-mount footprint. Further evaluation was also performed using the latest pulser board  
 527 prototype once they had arrived.

528 Following comparative performance evaluations, the configuration using the EPC8004  
 529 switch was selected for continued use. While both the EPC8004 and EPC2012 switches  
 530 exhibited similar electrical characteristics, the EPC8004 offered superior performance due to  
 531 its lower parasitic capacitance, without any additional cost. The pulser board assembly was  
 532 housed within a dark box during testing, and a 3D-printed fibre coupler was employed to  
 533 facilitate light delivery. The initial focus of the evaluation was on the shape of the generated  
 534 optical pulse. During component selection, it was observed that the LED previously sourced  
 535 from Mouser (ATS2012UV385 by Kingbright) provided acceptable performance in terms of  
 536 electrical characteristics, but the optical output was suboptimal, as it was showing a strange  
 537 “double pulsing”, which can be seen in Figure 32. Additionally, this LED was found to be  
 538 out of stock and obsolete at the time after testing, precluding further procurement.

539 Subsequently, four ultraviolet LEDs from LC LED were assessed—two emitting at 365 nm  
 540 and two at 395 nm—each in both 0805 and 0603 surface-mount packages. Results demon-  
 541 strated that the 0805 package LEDs provided significantly better optical coupling efficiency  
 542 with the FP400URT optical fibre. Furthermore, the 365 nm variant exhibited superior opti-  
 543 cal power output relative to the 395 nm counterparts. Based on these findings, the LC LED  
 544 UT-67UV365P [15] 365 nm LED was selected as the most suitable LED for this application.  
 545 Tests showed the LED behaved well, providing an optical pulse of 2.8 ns width, with  
 546 3.3 ns electrical signal, as shown as Figure 33. The pulse width deviation is 60.218 ps, or  
 547 2.12% , and the histogram shows the pulse distribution.

548 A long-term stress test was also performed for this LED. The pulser system was placed  
 549 in a small dark box, and a new 365 nm LED was soldered onto the pulser board. The pulse  
 550 frequency was set to 30 kHz, and the pulse width was set to 2.8 ns, which yielded a 6.8 ns  
 551 pulse after dispersion through 180 m of fibre. The system was running continuously for 13

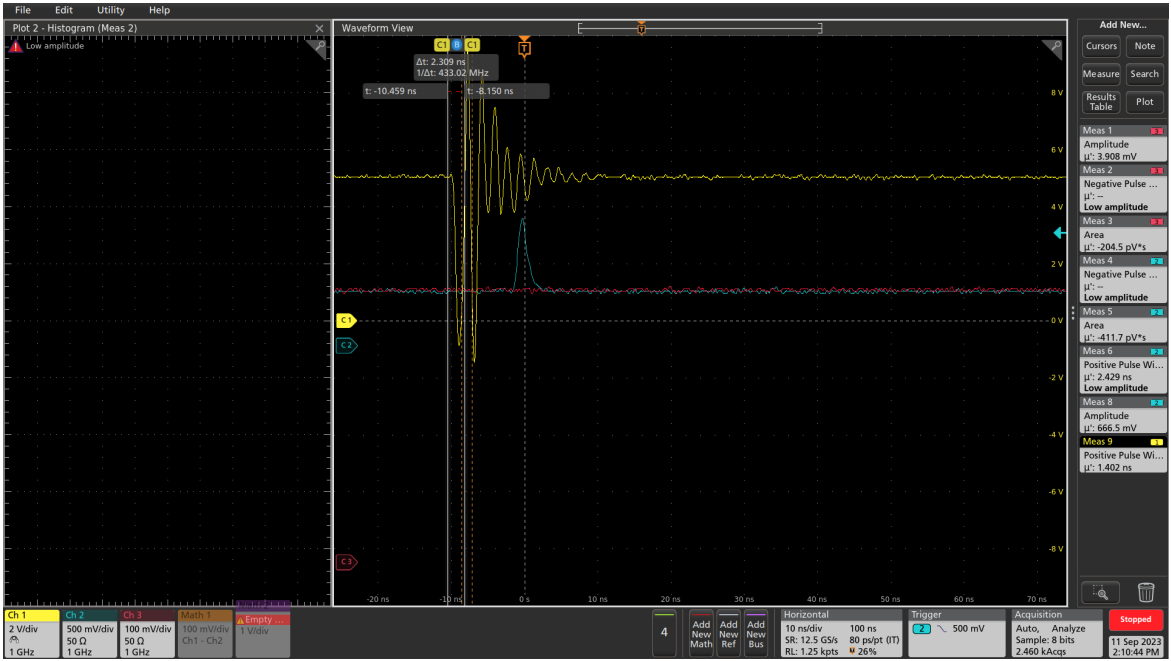


Figure 32: Double pulse observed from the Kingbright ATS2012UV385 LED.

552 days, during which power and air temperature measurements were made every 10 seconds.  
 553 The air temperature was measured at the power meter, using the Thorlabs PM100USB.  
 554 Each individual LED is expected to run at around 0.0082 Hz, as the auto-calib process is  
 555 expected to pulse any channel at 1 Hz rate and there are 122 active channels. This means  
 556 that pulsing the LED at 30 kHz for 13 days is equivalent to 106,849 years of normal running,  
 557 not including the short dedicated calibration runs where the system will run at 1 kHz. While  
 558 results are not calibrated for temperature change, it can be seen that most changes in power  
 559 correlate with temperature fluctuations. By comparing power results for the same ambient  
 560 temperature at the beginning and end of the experiment, a 1.5% loss in power is observed.

## 561 7.4 LVDS to TTL Converter

562 The DS90C402 [16] from Texas Instruments was selected as the LVDS-to-TTL conversion  
 563 solution. This device is a dual-channel converter, chosen primarily for its fast switching  
 564 characteristics—offering both rise and fall times of approximately 500 ps. It operates at  
 565 5 V and provides 5 V TTL output levels, which aligns well with the requirements of the  
 566 downstream switching circuitry. The inclusion of two channels is particularly advantageous,  
 567 as it enables the generation of sub-nanosecond differential pulses by precisely offsetting the  
 568 channels, as described in Switch Selection. Among commercially available devices with  
 569 these specifications, the DS90C402 is the fastest and is readily available through multiple  
 570 distributors.

571 The associated circuit was implemented in accordance with the manufacturer’s recom-  
 572 mendations provided in the datasheet. A decoupling capacitor was placed in close proximity  
 573 to the power supply pin to minimise voltage ripple. Output traces were routed using polygon  
 574 fills to reduce impedance and enhance signal integrity, and a continuous ground plane was  
 575 placed beneath the signal layers to improve shielding and minimise electromagnetic interfer-  
 576 ence. The schematic for this is given in Figure 35.

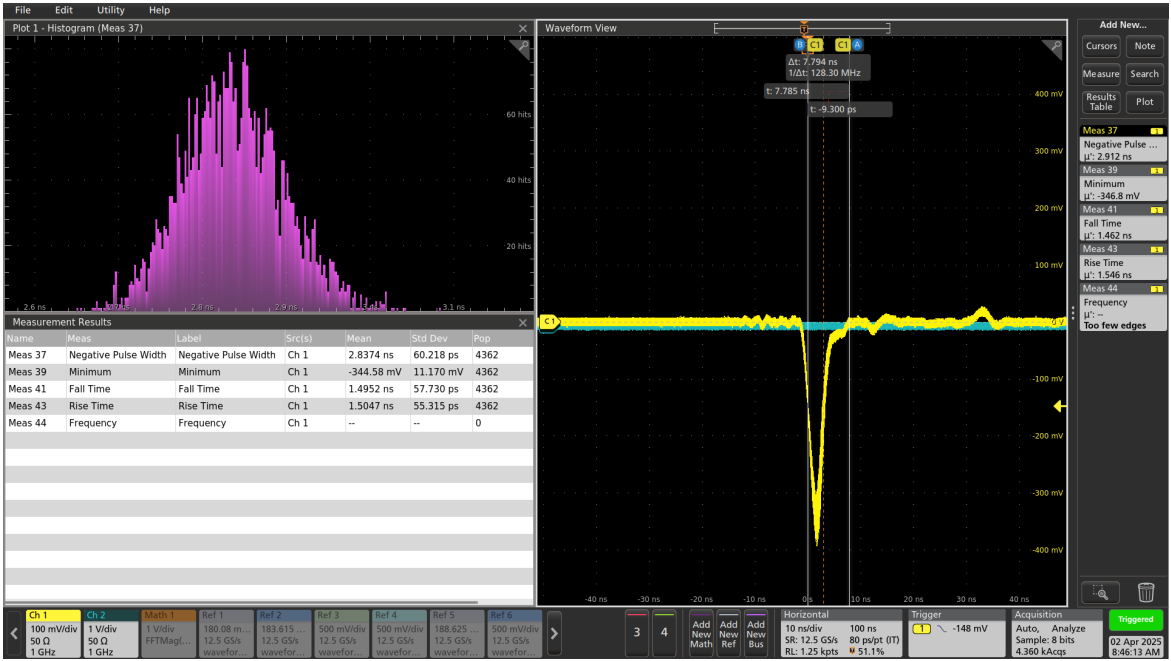


Figure 33: Scope trace and pulse width histogram for a 3.3 ns input signal, through a 1 m FP400URT fibre.

## 577 7.5 Power Supplies

578 Each pulser board is required to incorporate a variable voltage power supply dedicated  
 579 to driving the LED, with an adjustable output range from 3 V to 12 V. This supply is  
 580 used exclusively to modulate the LED’s light output by varying the forward voltage, and  
 581 consequently the current. The design specification also necessitates that the power supply  
 582 be remotely controllable—i.e., capable of being switched on or off via a simple logic-level  
 583 signal.

584 For this purpose, the LT1963A [17] adjustable low-dropout linear regulator was selected.  
 585 This regulator has demonstrated reliable performance in previous pulser board iterations  
 586 and offers a favourable balance of cost-effectiveness and controllability. The implementation  
 587 includes standard filtering and decoupling, with layout details provided in Figure 36. The  
 588 schematic provided in Figure 37 is an early version used for prototyping; the adjustable  
 589 circuit has been simulated and will be tested shortly, and the enable circuit has been tested,  
 590 modified and simplified. Updated schematics will be provided with v1.0 circuit. There will  
 591 be overcurrent protection built in to the system as well. A ZXCT1051 (Reference!) is used  
 592 to monitor the current and if it senses larger than normal current then it send a signal to  
 593 the FPGA to turn the damaged board off. A surface mounted fuse will be added in line as  
 594 well to make sure there is a second line of defense as well.

595 In addition to the variable LED supply, each board requires a stable 5 V supply to power  
 596 both the DS90C402 LVDS-to-TTL converter and the LMG1020 gate driver. Unlike the LED  
 597 supply, this rail remains continuously powered. The 5 V supply is provided by an LM2937-5  
 598 [18], a fixed-output linear voltage regulator, which has been successfully employed in various  
 599 high-speed and low-noise applications within the laboratory. The associated circuit schematic  
 600 and layout and schematic are shown in Figures 38 and 39 respectively.

601 To meet system-level design constraints, each pulser board is equipped with its own  
 602 independent 12 V input supply, ensuring that LED output intensity can be individually  
 603 controlled on a per-board basis. However, the 5 V supply is common across all boards

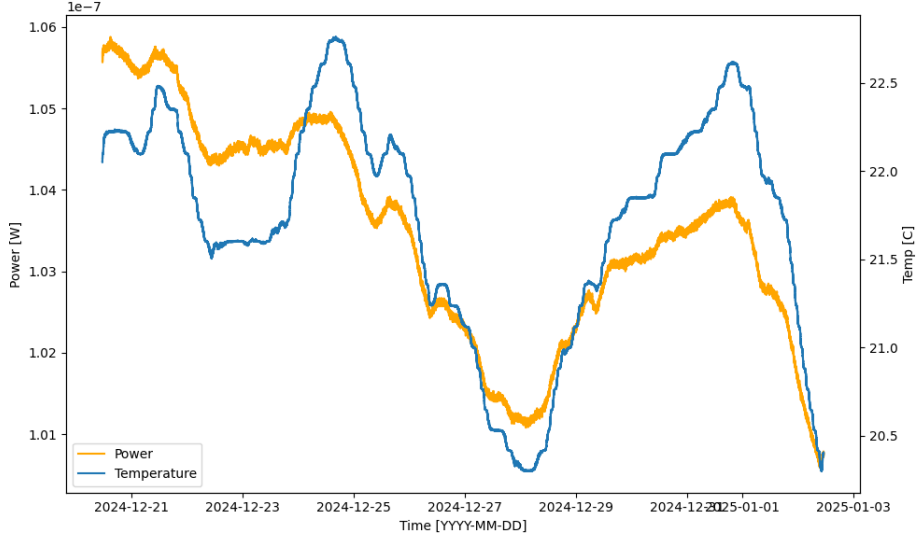
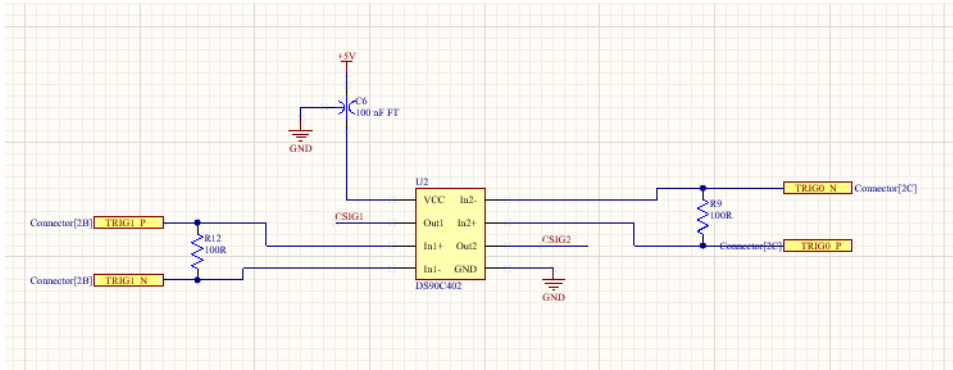


Figure 34: LED power and ambient temperature as a function of time for the long term tests.



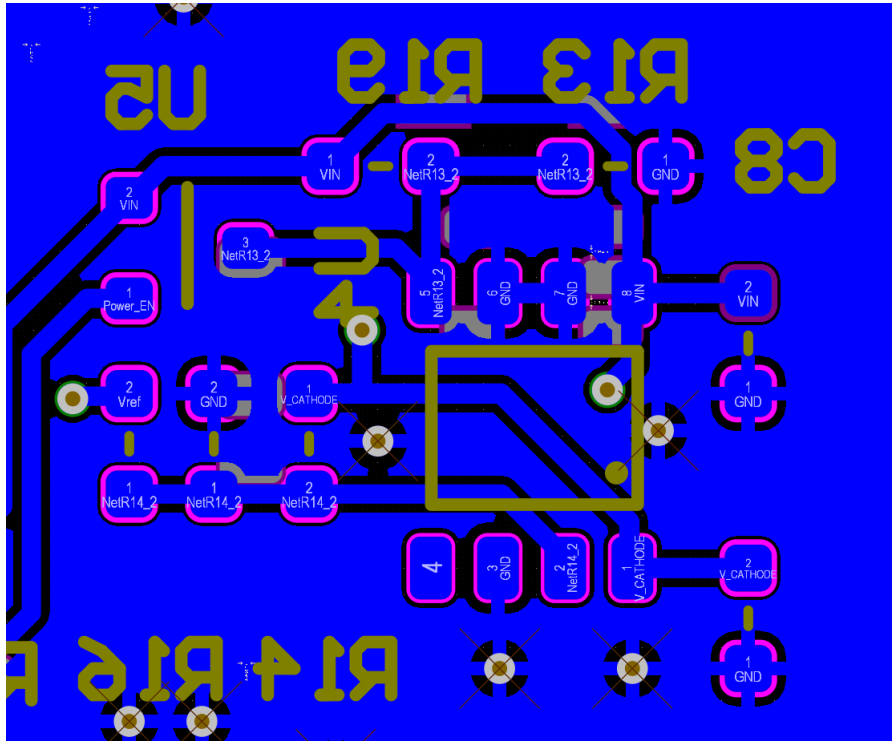


Figure 36: LT1963 Layout

cost-effective, priced at approximately £0.50 per unit, with wide availability ensuring ease of procurement. Multiple height variants are available within the same series, facilitating flexible mechanical integration within the Eurocard crate system. The compact footprint of the connector allows for a reduced PCB form factor. Electrically, the high-frequency performance supports reliable LVDS signal transmission. Additionally, the compact footprint of the connector is well-suited to space-constrained PCB layouts.

An illustration showing the connector and corresponding circuit layout is provided in Figure 40.

## 7.7 Fibre Coupler

During the prototyping phase, improvements were made to the PCB layout to better accommodate a fibre coupler. As a result, the current design includes provisions for precise mechanical mounting and alignment. Specifically, two mounting holes for M2 screws have been incorporated, enabling the 3D-printed coupler to be firmly secured to the board (see Figure 41). In addition, two dowel holes have been added to guide the coupler into position, ensuring accurate alignment over the LED. Given the tolerances associated with PCB fabrication and 3D printing, an alignment accuracy of approximately 100 µm is expected.

To optimise the electrical path, capacitors have been repositioned as close as possible to the LEDs. This minimises parasitic inductance and resistance, while enabling a centralised layout of larger components. The resulting configuration creates a compact chamber housing both the LEDs and associated capacitors.

The design for the fibre coupler is modular, consisting of three components: a base section mounted to the pulser PCB, a top section into which the fibres will be epoxied, and an intermediate attenuator element. The latter part will be added to the current design to space the fibre from the LED and thereby adjust the optical coupling efficiency to achieve required attenuation, accounting for the different lengths of fibre in the system. This means

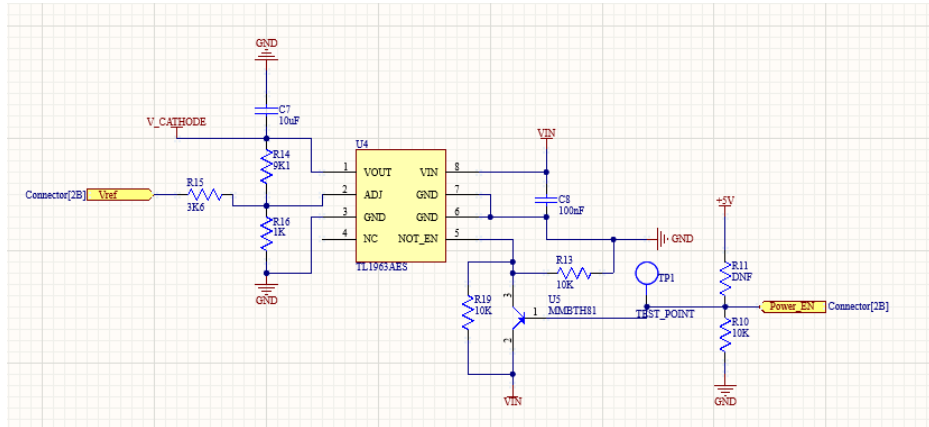


Figure 37: 12V Circuit Schematics

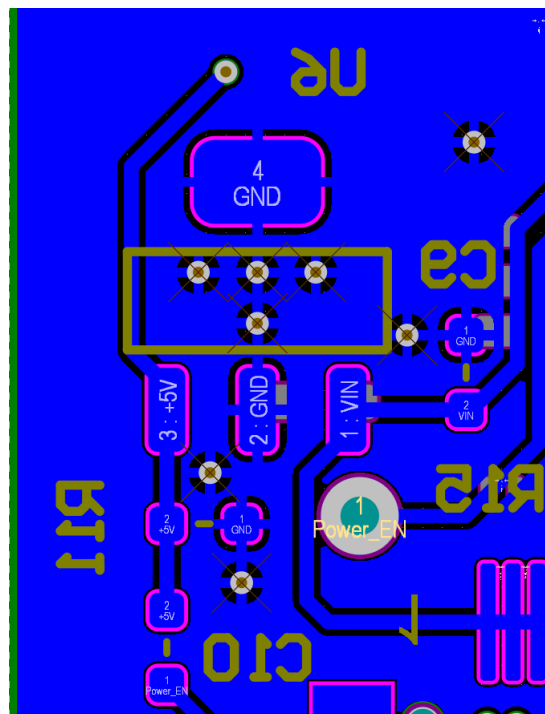


Figure 38: LM2937-5 Layout

the attenuation will be implemented within the coupler itself, allowing the LED output to remain within the electronically controlled dynamic range.

The fibre coupler will be fabricated via stereolithography (SLA) using a black resin to minimise light transmission through the material. Additional light-tight testing will be conducted, and black paint may be applied if further sealing is required. Furthermore, laser-cut rubber gaskets will be introduced at interface points to ensure optimal optical isolation and mechanical sealing.

## 7.8 Photon Yield Tests

As discussed in Section 2, one of the primary requirements of the OD diffuser system is to saturate as many of the OD PMTs as possible. To that end, an important test of the LED pulser electronics and candidate LEDs was determining the maximum photon output.

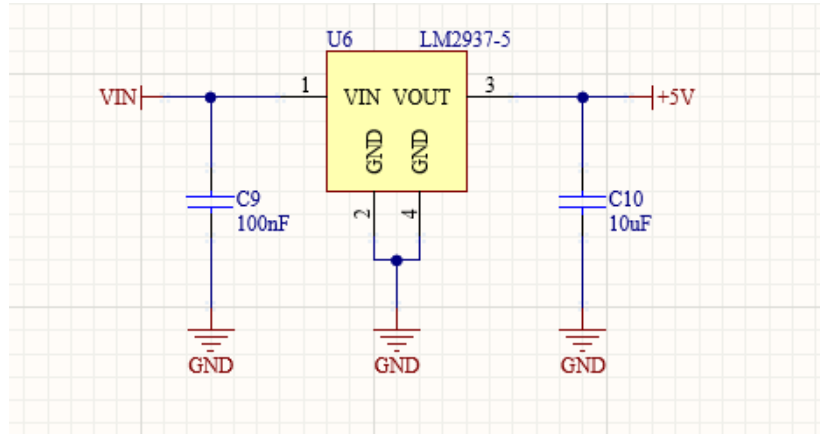


Figure 39: 5V circuit schematics

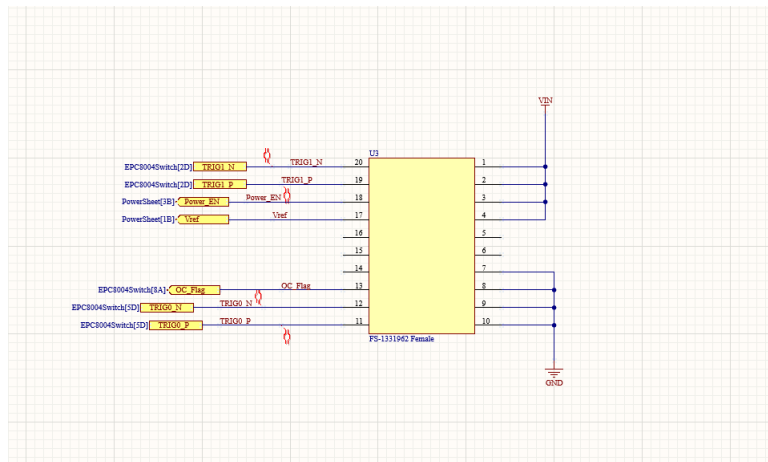


Figure 40: Connector Schematics

656 To provide a realistic amount of attenuation and dispersion, several FP400URT fibres  
 657 were connected in series using Thorlabs ADAFC1 FC-FC mating sleeves. Combining a 1 m  
 658 patch fibre with a 35 m, 40 m and 105 m reel equated to a total of 181 m with three mating  
 659 sleeves,  $\sim$ 10 m greater than the expected maximum fibre distance in reality. One end of the  
 660 chain of fibres was connected to the LED board via a prototype fibre coupler, which holds  
 661 the fibre end directly against the LED. To improve collection efficiency, the cavity was filled  
 662 with Thorlabs G608N3 index matching gel. The other end of the fibre chain was connected  
 663 to either a Hamamatsu H10721-210 PMT or a Thorlabs PM100USB with a S150C sensor,  
 664 for timing or power measurements respectively.

665 The LED board was set at 12 V, the current highest voltage output. The fibre was first  
 666 connected to the PMT, to confirm that the pulse width was sub-10 ns. The power was then  
 667 measured by the power meter. From this test, the maximum recorded light yield was found  
 668 to be  $2.4 \times 10^7$  photons per pulse. Further data was taken to investigate the dynamic range  
 669 associated with changing pulse width and voltage, however in migrating lab PCs this has  
 670 been lost, and will be retaken with the most recent versions of the hardware. Despite this,  
 671 these numbers show that the system is capable of producing a large number of photons per  
 672 pulse (ppp). In Section 4 an output of  $2 \times 10^7$  ppp was shown to yield up to 86% saturation  
 673 in the barrel region.

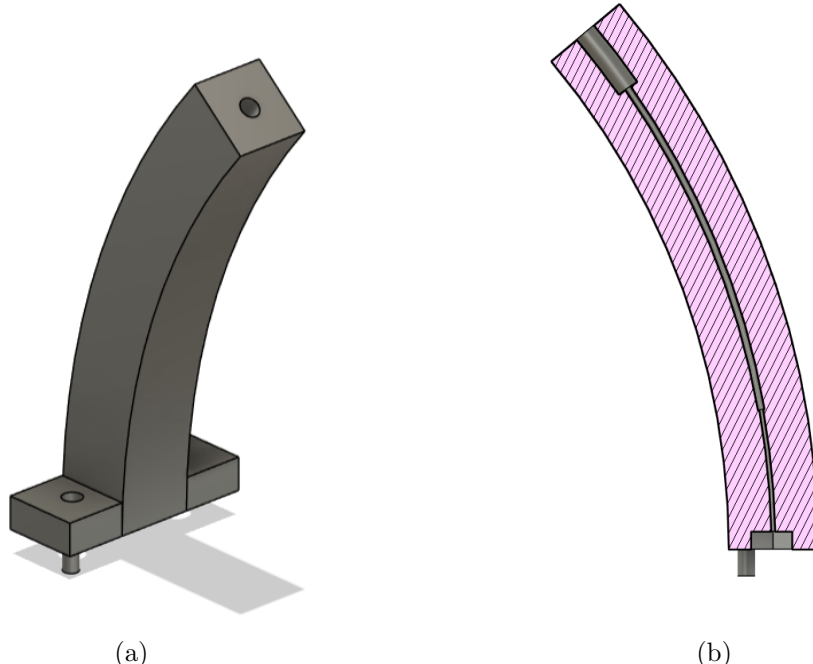


Figure 41: Fibre coupler design, showing (a) the coupler from the outside and (b) a cross-section. The coupler sits directly over the top of the surface-mounted LED.

## 674 7.9 Production

675 Production will be carried out using PCB Train as they are local and competitively priced,  
 676 and known to produce boards of good quality. Estimated cost is £12.27 per board, which  
 677 equates to £1,496.94 for 122 units or £1,840.5 for 150 units, and production is £4073.48 for  
 678 122 units for 15 days lead time, or £3985 for 150 units at 25 days lead time. The full cost  
 679 breakdown is shown in Figure 42

## 680 7.10 Changes Expected from v0.9 to v1.0

### 681 7.10.1 LED and Switching Circuit

682 There will be minimal changes to the LED and switching circuit. Changes will be made to  
 683 the position of the switching devices, placing them slightly closer to each other to reduce  
 684 transmission line length. The LED will likely remain as the LC LED UT-67UV365P 365nm  
 685 0805 LED, but further LED tests will be performed. This takes a short amount of time, and  
 686 may lead to discovering better LEDs in the future which would be easy to swap in due to  
 687 standardised footprints.

### 688 7.10.2 LVDS-to-TTL Converter

689 No changes are expected to this circuit.

### 690 7.10.3 Power Supplies

691 Reverse voltage bias will be removed as no difference between normal and reverse bias was  
 692 observed photon output. The overcurrent protection and power enable circuit will be re-  
 693 worked.

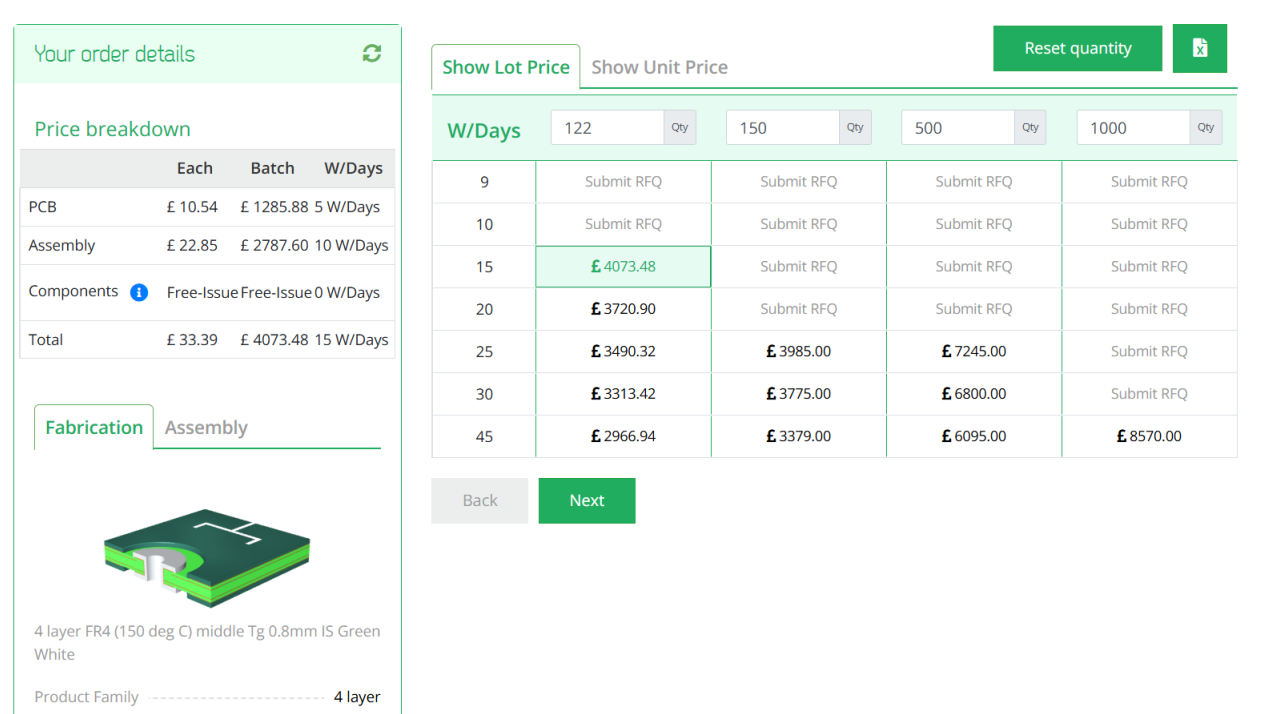


Figure 42: PCBTrain PCB production and assembly costs

#### 694 7.10.4 Connector

695 No changes are expected to this.

#### 696 7.10.5 Fibre Coupler

697 A brand new fibre coupler will be designed due to the recent requirement changes regarding  
698 the different fibre lengths.

## 699 8 Server Rack and Cooling

700 To house the electronics for the LI systems, two 42U server racks with 800 mm depth will  
701 be used. The front of the server rack will be used for electrical connections and displays,  
702 and the reverse/internal will be used only for fibre routing. The server racks will include  
703 Uninterruptible Power Supplies (UPS) for safe power delivery and for power processing, to  
704 avoid issues with potential instabilities in the main power supply. Each rack will include an  
705 air conditioning unit to have a controlled temperature and remove humidity from the air,  
706 as the relative humidity in the air is expected to be above 70%. Although specific tests on  
707 running the LED electronics in humid conditions have not been carried out, it is known that  
708 the optical switches for the laser calibration system requires lower humidity levels. In order  
709 to simplify things and remove the potential of humidity issues with the LED electronics,  
710 both server racks will be air conditioned. These systems are widely available and will be  
711 chosen closer to installation.

## 712 9 LED Monitoring

713 To monitor the light output from the LEDs before attenuation by fibres and convolution  
714 with water parameters, PMTs will be placed near to the LED sources. This is a similar  
715 design to what is currently used in the Super-K UKLI system. Each LED connector will  
716 feature a second fibre to take light to a series of PMTs, which are expected to be Hamamatsu  
717 H10721-210. Due to the 8 mm diameter of the PMT window, up to 16 fibres can be attached,  
718 meaning one PMT can monitor up to 16 LED boards at once. Each PMT will be powered  
719 by a unique low cost power supply developed for the SK UKLI system. These will be housed  
720 in a small 2–3 U server rack. The signals from the PMTs will then go to the dedicated HK  
721 electronics channels that are set up for monitoring.

## 722 10 Control System for LEDs

723 The LEDs are driven by a differential LVDS signal originating from the FPGA. The FPGA  
724 in use is the Genesys 2 [20] development board, which operates a pulsing VHDL module  
725 clocked at 300 MHz. Pulses are generated on the rising edge of this clock, and toggling the  
726 output (i.e., asserting and then deasserting the trigger) requires a minimum of two clock  
727 cycles. Consequently, the shortest achievable pulse duration in this configuration is 3.3 ns.

728 One of the main limitations of this setup is the coarse time resolution: pulse durations  
729 are effectively constrained to integer multiples of 3.3 ns. To achieve a broader and more  
730 finely resolved spectrum of optical injection into the detector, improved temporal precision  
731 is necessary. This is accomplished using the Xilinx IODELAY primitive, originally designed for  
732 high-speed interface timing alignment. The IODELAY module permits fine-tuning of signal  
733 timing to account for PCB trace mismatches, and in this application, it is repurposed to  
734 introduce controlled delays between pulses.

735 To generate shorter pulses, two identical signals are created, one of which is delayed  
736 using IODELAY. These signals are then combined using a logical AND operation, producing  
737 a narrower pulse. Since the IODELAY module requires one clock cycle to process the input,  
738 both signals—regardless of whether they are delayed—must pass through an IODELAY stage  
739 to ensure temporal synchronisation.

740 Conversely, to produce longer pulses, the same methodology is applied, but the signals are  
741 combined using a logical OR gate instead. This approach extends the pulse width beyond the  
742 base clock resolution, enabling pulse durations ranging from approximately 1.5 ns to 4.5 ns  
743 in 49 discrete steps. The lower bound is determined by the threshold of the LVDS-to-TTL  
744 converter, which does not respond to pulses shorter than approximately 1.5 ns .

745 For channels using the longest optical fibres, this extended range is sufficient, given  
746 the intrinsic dispersion in the fibre optics of around 5 ns. However, shorter fibres require  
747 additional pulse shaping. To this end, an additional mechanism is implemented using a for  
748 loop structure within the FPGA logic. This allows the pulse to persist for multiple clock  
749 cycles, effectively producing longer pulses by repetition. However, due to FPGA architecture  
750 constraints, each iteration of the loop consumes a clock cycle, necessitating careful timing  
751 control. For instance, to produce a 6.6 ns pulse, the loop must be configured for two cycles,  
752 accounting for the loop overhead.

753 Further refinement is under investigation through the daisy-chaining of multiple IODELAY  
754 modules. This would enable sub-nanosecond granularity by introducing additional interme-  
755 diate delay steps. While promising, this technique requires further validation and testing.

756 The pulse control data structure is currently under development. There are two types  
757 of pulse description considered. In the first option, the software interface would require two  
758 parameters per channel: a *coarse* step and a *fine* step, reflecting the approach used in the SK

759 system. The other option would be just a single variable and then simple logic turning that  
760 variable into the *coarse* and *fine* step that the internal logic requires. Two hardware modules  
761 are planned: one for generating the single shortest possible pulse (to minimise latency), and  
762 another for multi-cycle pulses using programmable duration. A selection logic will assess the  
763 input and route it to the appropriate module based on the desired pulse characteristics.

764 Each LED channel will be controlled independently, allowing for unique pulse configura-  
765 tions across channels. The global trigger will be derived from the system clock, and each  
766 channel will pulse in a predefined sequence while triggered from the global trigger. This  
767 architecture also supports simultaneous pulsing of multiple channels. Should asynchronous  
768 behaviour be required, additional per-channel delay logic can be implemented. Given the  
769 five distinct fibre lengths used in the system, each channel group will also include a config-  
770 urable delay offset to compensate for propagation time differences. These group delays will  
771 be calibrated and fixed, with the option of fine-tuning individual channels post-deployment  
772 if necessary.

773 The repetition rate can be adjusted as well, including a single pulse, using external  
774 trigger, from 0.001Hz through 1 kHz to multiple megahertz if needed, but the system was  
775 only tested up to 30 kHz, as that was a high enough rate to illuminate the power monitor's  
776 sensor.

777 The FPGA programming remains in active development. Inter-crate communication  
778 protocols and synchronisation are currently under integration and testing.

## 779 11 Crate Electronics

### 780 11.1 Overview

781 The system specification calls for control of up to 122 LED channels, significantly exceeding  
782 the channel counts used in current systems such as Super-Kamiokande or LUX-ZEPLIN,  
783 which the previous generation of pulser boards are used for. To manage this complexity, the  
784 design prioritises ease of use, maintainability, and straightforward deployment, particularly  
785 given that the server racks will accommodate hundreds of optical fibres.

786 To achieve this, a system concept originally developed by ATLAS collaborators (specifi-  
787 cally by Ashley Greenal) has been adapted. The original design utilises a Genesys 2 FPGA  
788 integrated into a half-width Verotec KM6-2 [21] Eurocard-compatible crate for testing pur-  
789 poses. This concept has been extended to a full 19-inch rack width, enabling the integration  
790 of up to 36 pulser boards within a single crate.

791 Each FPGA is capable of interfacing with up to 38 pulser boards, thereby maximising  
792 the utilisation of available LVDS differential pairs, with an additional pair reserved for the  
793 laser trigger signal. This configuration ensures full use of the Genesys 2's I/O capacity while  
794 maintaining flexibility for future expansion.

795 The system architecture consists of three primary components: the Blade (Section 11.2),  
796 Backplane (Section 11.3) and Eurocard (Section 11.4). This modular approach ensures  
797 scalability and facilitates debugging, replacement, and upgrades. It also provides a robust  
798 foundation for managing high channel counts while maintaining signal integrity and synchro-  
799 nisation across the system.

800 The system will consist of four crates, which allows for up to 144 pulser boards. The  
801 OD diffuser system requires 122 boards to run, and the auto-Xenon calibration system is  
802 expected to use one or two of the additional boards. This means there will be 20 spare boards  
803 available for hot-swapping. These can be further grouped into five sets of four, to have four  
804 spare boards for each of the five different fibre lengths. Should issues arise, a local technician  
805 can remove the signal and monitor fibres from the broken pulser board, attach them to a

806 spare board, and reconfigure the software to use the spare board for running, all with remote  
807 expert guidance. The next time an expert is on site they can do further maintenance or  
808 repair if needed.

## 809 11.2 Blade

810 The Blade is a simple, eight layer board, that has a SEAM-40-06.5-L-10-2-A-K-TR [22]  
811 connector which is a direct fit for the Genesys 2's FMC connector. It features a PCIE 16X  
812 connector at the edge for connectivity to the Backplane. The PCIE was selected by Ashley  
813 Greenal as it is a well documented standard connector and there are a large amount of  
814 connectors available that can be bought easily. While PCIE connectors are being used, the  
815 PCIE standards for communication are not. This is a very dense PCB with all the differential  
816 tracks on it, so buried vias and multiple layers will be used. See Figure 43 for a work in  
817 progress version.

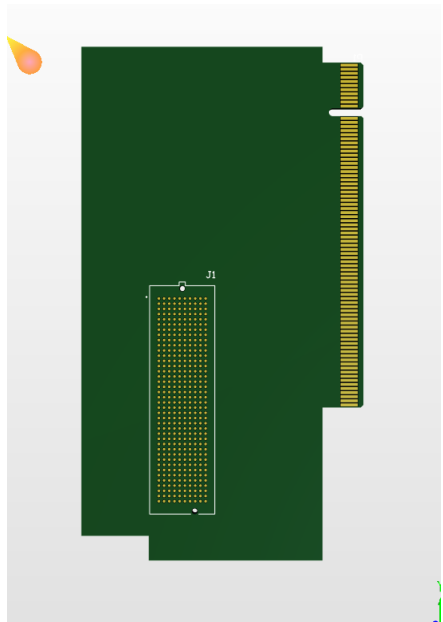


Figure 43: Blade Work in Progress

## 818 11.3 Backplane

819 The Backplane serves two primary functions: the distribution of differential signals from the  
820 Blade to the Eurocards, and the reception and distribution of power throughout the crate  
821 system. It accepts external power inputs of 12 V and  $\pm 5$  V, and includes a basic regulation  
822 circuit to stabilise these supply voltages for downstream use.

823 Given the mechanical constraints and routing complexity, the Backplane is implemented  
824 as a four-layer PCB with impedance-controlled traces to ensure signal integrity across all  
825 differential pairs. It features a single PCIe x16 connector to interface with the Blade, and  
826 three PCIe x8 connectors to interface with the Eurocards.

827 The Eurocards are positioned at slots 2, 8, and 64 within the crate. This arrangement  
828 creates two symmetrical chambers with 48 units spacing between cards, ensuring adequate  
829 space to accommodate the minimum long-term bend radius of the FP400URT optical fibres.  
830 This layout balances mechanical reliability with signal routing efficiency and supports long-  
831 term maintainability of the system. See Figure 44 for a work in progress version.

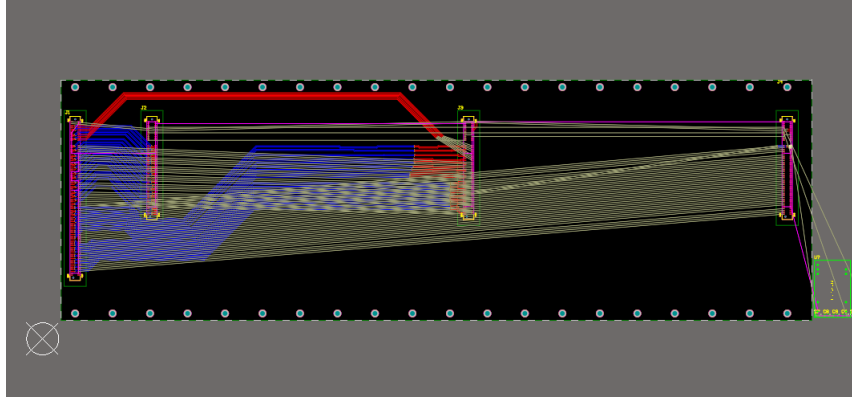


Figure 44: Backplane Work in Progress

#### 832 11.4 Eurocard

833 The Eurocard format defines the physical and electrical standard for the crate system, hence  
 834 the naming convention. Each Eurocard is equipped with a PCIe x8 connector for interfacing  
 835 with the Backplane, and is designed to host up to 18 pulser boards—nine mounted on each  
 836 face. Pulser boards connect via FS-1332120 Male[23] connectors, and each socket includes  
 837 two mounting holes for mechanical standoffs.

838 The board layout on each side consists of two staggered rows: five sockets in the back  
 839 row and four in the front. The two faces are laterally offset by approximately 10 mm to  
 840 prevent interference or fibre clashes when the system is fully populated and enclosed within  
 841 the crate chamber. This offset ensures smooth fibre routing and accommodates the bend  
 842 radius requirements of FP400URT fibres.

843 Power distribution within each Eurocard is handled by a THD 12-1212 [24]12 V DC-DC  
 844 regulator. This regulator provides local power isolation for the pulser boards and includes  
 845 a control pin connected to a PCA9698 [25] 40-pin GPIO expander. This allows for system-  
 846 level control, enabling or disabling all pulser boards on a card—an essential feature during  
 847 power-up, especially when the FPGA may inadvertently drive all differential outputs high  
 848 during reprogramming.

849 The GPIO expander is responsible for enabling the local 12 V regulator and for selectively  
 850 powering individual pulser boards. This facilitates fault isolation and power savings in  
 851 channels that are inactive or disconnected. Additional GPIO pins are assigned to monitor  
 852 output voltage levels via the overcurrent sensing circuitry.

853 To provide per-channel LED power control, an AD5673 [26] DAC is included. It out-  
 854 puts analogue control voltages to the onboard adjustable regulators on each pulser board,  
 855 allowing for independent LED drive voltage per channel. Both the GPIO and DAC devices  
 856 communicate with the system over the I<sup>2</sup>C protocol.

857 For laser synchronisation, the Eurocard includes a differential-to-NIM conversion stage.  
 858 This consists of an LVDS-to-TTL converter identical to that used on the pulser boards,  
 859 followed by a TTL-to-NIM converter. This ensures compatibility with legacy NIM-based  
 860 timing systems used in external laser triggering. See Figure 45 for a work in progress version.

## 861 12 Summary

862 This document has presented the development of a calibration system for the Hyper-K OD,  
 863 focussing primarily on the array of diffusers which are powered by custom designed LED  
 864 pulser boards. Through a series of optimisations, a maximum yield of  $2.4 \times 10^7$  photons per

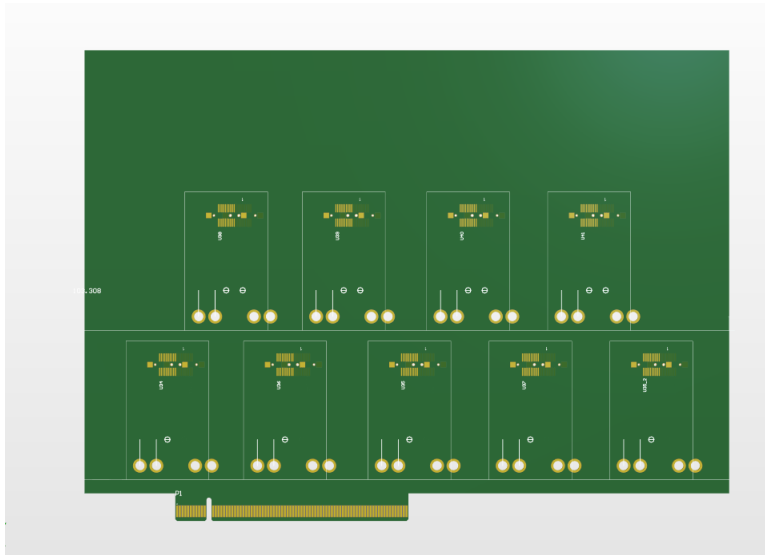


Figure 45: Eurocard Work in Progress

865 pulse is obtained, after attenuation by 181 m of fibre optic cable with multiple connectors.  
 866 This is achieved while keeping the pulse width under 10 ns, which was a design requirement.  
 867 Saturation studies performed using Monte Carlo simulation show that this is sufficient to  
 868 saturate the majority of OD PMTs, with up to 86% of PMTs in the barrel region within the  
 869 saturation limit for  $10 \times 10^6$  injected photons per pulse out of the diffuser. The electronics  
 870 used to produce the mentioned light pulses are in a mature state of design, with board  
 871 production expected to begin in the near future.

872 Results are also presented on the sensitivity of OD collimators to changes in absorption,  
 873 Rayleigh scattering, and Tyvek reflectivity. These suggest that for a barrel collimator  
 874 sensitivity at the 99% confidence level can be achieved for changes in reflectivity at the  
 875 sub-percent level, a reduction in the absorption length of 20% can be detected at the 95%  
 876 confidence level, and a change in the scattering length can be detected at the 99% confidence  
 877 level within a few percent of the nominal value.

## 878 References

- 879 [1] S. Jenkins *et al.*, “HK LI Fibre Specifications,” HK-TN-0091, Aug. 2025.
- 880 [2] Thorlabs. “FP400URT Datasheet.” (2022), [Online]. Available: <https://www.thorlabs.com/drawings/7ade35b092fac3f3-EFB2F350-971A-B4B4-29D36C92039FB538/FP400URT-SpecSheet.pdf> (visited on 07/17/2025).
- 881 [3] Hyper-Kamiokande Outer Detector Group: D. Lodovico, E. Drakopoulou, G. Erofeev,  
 882 *et al.*, “Outer detector technical report,” HK-TN-0064, 2022.
- 883 [4] H.-K. Collaboration. “WCSim Version 1.12.26.” (2018), [Online]. Available: <https://github.com/WCSim/WCSim/releases/tag/v1.12.26> (visited on 09/16/2025).
- 884 [5] S. Boyd *et al.*, “Hyper-Kamiokande light injector diffuser technical note,” HK-TN-0042,  
 885 May 2023.
- 886 [6] N. E. M. Association. “NEMA STANDARDS PUBLICATION NO. LI 1-1998.” (1998),  
 887 [Online]. Available: <https://www.nema.org/docs/default-source/standards-document-library/li1.pdf> (visited on 08/19/2025).

- 892 [7] I. T. AG. “BFR 92P E6327 Datasheet.” (2009), [Online]. Available: [https://www.mouser.co.uk/datasheet/2/196/Infineon\\_LNA\\_BFR92P\\_14-73949.pdf](https://www.mouser.co.uk/datasheet/2/196/Infineon_LNA_BFR92P_14-73949.pdf) (visited on 07/17/2025).
- 893 [8] T. I. Incorporated. “LMG1020 Datasheet.” (2018), [Online]. Available: [https://www.ti.com/lit/ds/symlink/lmg1020.pdf?ts=1752716909774&ref\\_url=https%253A%252F%252Fwww.mouser.cn%252F](https://www.ti.com/lit/ds/symlink/lmg1020.pdf?ts=1752716909774&ref_url=https%253A%252F%252Fwww.mouser.cn%252F) (visited on 07/17/2025).
- 894 [9] N. Braam *et al.*, “LED-mPMTs for hyperK,” HK-TN-0052, Oct. 2023.
- 895 [10] E. P. C. Corporation. “EPC2012 Datasheet.” (2012), [Online]. Available: [https://epc-co.com/epc/Portals/0/epc/documents/datasheets/EPC2012\\_datasheet.pdf](https://epc-co.com/epc/Portals/0/epc/documents/datasheets/EPC2012_datasheet.pdf) (visited on 07/17/2025).
- 896 [11] E. P. C. Corporation. “EPC8004 Datasheet.” (2023), [Online]. Available: [https://epc-co.com/epc/Portals/0/epc/documents/datasheets/EPC8004\\_datasheet.pdf](https://epc-co.com/epc/Portals/0/epc/documents/datasheets/EPC8004_datasheet.pdf) (visited on 07/17/2025).
- 897 [12] Kingbright. “ATS2012UV385 Datasheet.” (2021), [Online]. Available: <https://www.mouser.co.uk/datasheet/2/216/ATS2012UV385-1374632.pdf> (visited on 07/17/2025).
- 898 [13] H. P. K.K. “H10721-210 Datasheet.” (2024), [Online]. Available: [https://www.hamamatsu.com/content/dam/hamamatsu-photonics/sites/documents/99\\_SALES\\_LIBRARY/etd/H10720\\_H10721 TPM01062E.pdf](https://www.hamamatsu.com/content/dam/hamamatsu-photonics/sites/documents/99_SALES_LIBRARY/etd/H10720_H10721 TPM01062E.pdf) (visited on 07/17/2025).
- 899 [14] E. P. C. Corporation. “Design of High Current Nanosecond Resonant Pulse Drivers for Laser Diodes, Lidar, and other Applications.” (2025), [Online]. Available: <https://epc-co.com/epc/Portals/0/epc/documents/application-notes/AN032%20Design%20of%20High%20Current%20Nanosecond%20Resonant%20Pulse%20Drivers.pdf> (visited on 07/17/2025).
- 900 [15] L. LED. “ut-67uv365p Datasheet.” (2018), [Online]. Available: <https://www.lc-led.com/products/ut-67uv365p.html> (visited on 08/21/2025).
- 901 [16] T. I. Incorporated. “DS90C402 Datasheet.” (2013), [Online]. Available: <https://www.ti.com/lit/ds/symlink/ds90c402.pdf> (visited on 07/17/2025).
- 902 [17] A. Devices. “LT1963 Datasheet.” (2021), [Online]. Available: <https://www.mouser.co.uk/datasheet/2/609/lt1963a-2256452.pdf> (visited on 07/17/2025).
- 903 [18] T. I. Incorporated. “LM2347-5 Datasheet.” (2014), [Online]. Available: <https://www.ti.com/lit/ds/symlink/lm2937.pdf> (visited on 07/17/2025).
- 904 [19] P. Contact. “1331962 Datasheet.” (2025), [Online]. Available: <https://www.phoenixcontact.com/en-us/products/smd-female-connectors-fs-0635-20-fv-r-40-1331962?type=pdf> (visited on 07/17/2025).
- 905 [20] Digilent. “Genesys 2 Datasheet.” (2017), [Online]. Available: [https://digilent.com/reference/\\_media/reference/programmable-logic/genesys-2/genesys\\_2\\_rm.pdf?srsltid=AfmBOorhD9699F1FTC059o719HmCW-0XnEORnRJf6Thzcvu0vMs-pbAf](https://digilent.com/reference/_media/reference/programmable-logic/genesys-2/genesys_2_rm.pdf?srsltid=AfmBOorhD9699F1FTC059o719HmCW-0XnEORnRJf6Thzcvu0vMs-pbAf) (visited on 07/17/2025).
- 906 [21] Verotec. “Verotec KM6-2 Datasheet.” (2017), [Online]. Available: <https://www.verotec.co.uk/tech-downloads/Section%201%20-%20KM6-II%20Subracks.pdf> (visited on 07/17/2025).
- 907 [22] Samtec. “SEAM-40-06.5-L-10-2-A-K-TR Datasheet.” (2025), [Online]. Available: [https://suddendocs.samtec.com/catalog\\_english/seam.pdf?\\_gl=1\\*1soskal\\*\\_gcl\\_au\\*0DQw0DM2MjE4LjE3NTI3NDg2NTY.\\*\\_ga\\*MTAxNjAx0TQwNS4xNzUyNzQ4NjU2\\*\\_ga\\_3KFNZC07WW\\*cxE3NTI3NDg2NTUkbzEkZzAkDE3NTI3NDg2NTUkajYwJGwwJGgw](https://suddendocs.samtec.com/catalog_english/seam.pdf?_gl=1*1soskal*_gcl_au*0DQw0DM2MjE4LjE3NTI3NDg2NTY.*_ga*MTAxNjAx0TQwNS4xNzUyNzQ4NjU2*_ga_3KFNZC07WW*cxE3NTI3NDg2NTUkbzEkZzAkDE3NTI3NDg2NTUkajYwJGwwJGgw) (visited on 07/17/2025).

- 938 [23] P. Contact. "1332120 Datasheet." (2025), [Online]. Available: <https://www.phoenixcontact.com/en-us/products/smd-male-connectors-fs-0635-20-mv-r-50-1332120?type=pdf> (visited on 08/21/2025).
- 939
- 940
- 941 [24] T. E. AG. "THD 12-1212 Datasheet." (2025), [Online]. Available: [https://www.tracopower.com/sites/default/files/products/datasheets/thd12\\_datasheet.pdf?t=1752706801](https://www.tracopower.com/sites/default/files/products/datasheets/thd12_datasheet.pdf?t=1752706801) (visited on 07/17/2025).
- 942
- 943
- 944 [25] N. B.V. "PCA9698 Datasheet." (2010), [Online]. Available: <https://www.nxp.com/docs/en/data-sheet/PCA9698.pdf> (visited on 07/17/2025).
- 945
- 946 [26] A. Devices. "AD5673 Datasheet." (2020), [Online]. Available: <https://www.analog.com/media/en/technical-documentation/data-sheets/ad5673r-5677r.pdf> (visited on 07/17/2025).
- 947
- 948